Evidence of Strong Upper Oceanic Crustal Hydration Outboard the Alaskan and Sumatran Subduction Zones

Tanner Acquisto, Anne Bécel, Satish C. Singh, Hélène Carton

JGR Solid Earth

RESEARCH ARTICLE
10.1029/2022JB024751

Evidence of Strong Upper Oceanic Crustal Hydration Outboard the Alaskan and Sumatran Subduction Zones

Tanner Acquisto[1], Anne Bécel[1], Satish C. Singh[2], and Hélène Carton[1,2]

[1]Lamont-Doherty Earth Observatory, Columbia University, Palisades, NY, USA, [2]Equipe de Géosciences Marines, Institut de Physique du Globe de Paris (CNRS, Université Paris Cité), Paris, France

Key Points:

- We present the first high-resolution estimates of upper crustal water content outboard two subduction zones
- Bending faults offshore Alaska hydrate the crust down to the mantle
- Complex deformation in the Wharton Basin hydrates upper crust which could explain a nearby slow slip event

Supporting Information:

Supporting Information may be found in the online version of this article.

Correspondence to:

T. Acquisto,
acquisto@ldeo.columbia.edu

Citation:

Acquisto, T., Bécel, A., Singh, S. C., & Carton, H. (2022). Evidence of strong upper oceanic crustal hydration outboard the Alaskan and Sumatran subduction zones. *Journal of Geophysical Research: Solid Earth*, *127*, e2022JB024751. https://doi.org/10.1029/2022JB024751

Received 13 MAY 2022
Accepted 12 SEP 2022
Corrected 14 OCT 2022 and 8 NOV 2022

This article was corrected on 14 OCT 2022 and 8 NOV 2022. See the end of the full text for details.

Author Contributions:

Conceptualization: Anne Bécel, Satish C. Singh, Hélène Carton
Formal analysis: Tanner Acquisto, Anne Bécel
Methodology: Tanner Acquisto, Anne Bécel, Satish C. Singh
Software: Tanner Acquisto
Validation: Tanner Acquisto
Writing – original draft: Tanner Acquisto, Anne Bécel, Satish C. Singh, Hélène Carton
Writing – review & editing: Tanner Acquisto, Anne Bécel, Satish C. Singh, Hélène Carton

Abstract The hydration state of subducting oceanic crust has been proposed to influence subduction zone processes like seismic coupling at the megathrust interface and arc magmatism downdip. Plate bending in the outer rise region is thought to help rehydrate the incoming oceanic lithosphere before subduction. Although numerous seismic refraction studies provide constraints on the amount of water stored in the lower crust and uppermost mantle, little information exists about how much free water is present in the upper 1–2 km of oceanic crust. Here, we present results from the application of advanced techniques to long-offset multi-channel seismic data acquired outboard the Alaskan and South Sumatran subduction zones. Our results show that the incoming upper crustal seismic layer, layer 2A, is significantly hydrated in both areas. Favorable conditions offshore the Alaska Peninsula promote the creation of a dense system of bending-related faults, facilitating the infiltration of fluids that increases average water estimates to ~3.9 wt.% H_2O in the outer rise. As the crust subducts and temperature increases, some free water may react with the host rocks to form mineral-bound water that is carried to greater depths, in agreement with elevated water contents found in arc lavas of Shumagin Gap volcanoes. Offshore Sumatra, we propose that similar layer 2A water estimates (~3.2 wt.% H_2O average) and heterogeneous hydration within 2B are associated with the ongoing, slow, complex deformation occurring in the Wharton Basin and thus potentially contribute to the presence of a long-lived slow slip event recently inferred there at seismogenic depths.

Plain Language Summary Convergent plate boundaries, where one plate subducts beneath the other, produce large and destructive earthquakes and tsunamis. The amount of water carried at a range of depths in the incoming plate is suspected to strongly influence processes that occur downdip, including the generation of earthquakes. However, little information is available on how the uppermost crust is hydrated and the amount of water present there before it subducts. To address this question, we utilize high-quality seismic data to provide some of the first estimates of the amount of free water in the upper ~1.2–2.3 km of oceanic crust outboard the Alaskan and Sumatran subduction zones. We find that the crust in these areas contains significant amounts of water in the pores and that rehydration of the crust before subduction may occur in different ways. Offshore Alaskan, the bending of the plate creates faults that allow more water to penetrate the crust which could be carried deep into the subduction zone. Offshore Sumatra, broad deformation of the incoming plate facilitates hydration without the need for strong bending. We propose these processes may influence the generation of long-lasting slow-slip events that have been recently inferred downdip.

1. Introduction

Most of the great destructive earthquakes occur along subduction boundaries (e.g., Davies et al., 1981). Water stored in the subducting oceanic lithosphere seems to play a fundamental role in fault slip behavior in the accretionary prism and along the megathrust (Bilek & Lay, 2018; Saffer & Tobin, 2011), as well as controlling deeper subduction zone processes such as arc magmatism and intermediate-depth earthquakes (e.g., Peacock, 1990). Quantifying the amount of water stored in the subducting lithosphere is also needed to better estimate the global water budget (e.g., Cai et al., 2018). Therefore, it is important to constrain the amount of water stored at all depths in the subducting lithosphere. Fluids (particularly seawater) are present in the pores of underthrusted sediments and oceanic crust as either free water or structurally bound in hydrous phases of mafic and ultramafic rocks (Faccenda, 2014; Peacock, 1990). The expulsion of pore fluids contained in sediments and upper oceanic crust occurs at relatively shallower depths (<30 km of the trench) and has been proposed to be a primary control of the generation of slow-slip events recorded in the shallow part of the subduction zone (Chesley et al., 2021; Mallick et al., 2021; Saffer & Tobin, 2011). Conversely, hydrous minerals stored in the crust and uppermost mantle

remain stable at greater temperatures and pressures and are released further downdip through dehydration reactions (Abers et al., 2017; Hacker et al., 2003; van Keken et al., 2011). Numerous previous studies have provided constraints on the amount of water in the lowermost oceanic crust and upper mantle outboard of subduction trenches (Ivandic et al., 2008; Shillington et al., 2015; Van Avendonk et al., 2011); however, few have been able to provide information about the hydration state of the upper oceanic crust (e.g., Canales et al., 2017; Chesley et al., 2021; Fujie et al., 2013; Naif et al., 2015). Robust constraints on the physical properties of subducting mature (>10 Myr) oceanic crust within and outside the bending area near the trench are central to developing a better understanding of subduction tectonics.

The highly porous upper section of the oceanic crust, termed layer 2, consists of extrusive lava flows and dikes, and could be 1–3 km thick (e.g., Christeson et al., 2019). Water is first introduced to layer 2 at mid-ocean ridges, where strong thermal gradients drive active circulation of seawater (Alt, 1995). Porosities in the uppermost crustal layer, layer 2A, can range between 25% and 50% (Arnulf et al., 2011) near the ridge, and are rapidly filled off-axis due to the precipitation of hydrous minerals (Wilkens et al., 1991). Whether hydrothermal circulation occurs as a closed or open system depends strongly on a combination of topographic forcings, the degree of abyssal hill faulting, and sedimentation rates (Nedimović et al., 2008; Newman et al., 2011). Farther off-axis, in crust older than 10 Myr, the continued precipitation of alteration minerals (though to a much lesser degree), changes in crack morphology, and/or the blanketing effect of sediments are believed to significantly hinder further active and open circulation of water (e.g., Carlson, 2010; Kardell et al., 2021; Nedimović et al., 2008). Kardell et al. (2019) show a gradual increase in layer 2A velocities up to 58 Ma, suggesting the persistence of low-temperature, passive hydrothermal circulation in slow-to intermediate-spread upper crust as old as 58 Myr from the South Atlantic. In a similar study by Audhkhasi and Singh (2019) in the equatorial Atlantic, no statistical increase in 2A velocities is observed beyond 4 Myr in slow-spread upper crust. Instead, the authors observe an increase in layer 2B velocities out to 46 Myr, which implies that passive hydrothermal circulation may occur below the 2A/2B boundary. While the uppermost oceanic crust has been drilled numerous times (e.g., Jarrard et al., 2003), most expeditions did not recover more than 300–400 m of basement. Two prominent exceptions are holes 504B and 1256D that, respectively sample ∼6 Myr old intermediate-spread and ∼15 Myr old superfast-spread oceanic crusts more than 1 km below the top of basement in the Cocos plate (e.g., Carlson, 2014a,b; Wilkens et al., 1991). Given the lack of drilling constraints, the most common techniques for elucidating composition and structure of oceanic crust are seismological; however, to date, very few high-resolution estimates exist for fast-spread mature upper crust, and therefore filling that gap is one of the objectives of this study.

For active circulation to take place in intraplate settings, the crust must be thinly sedimented or directly exposed to seawater through basement highs (e.g., seamounts; Newman et al., 2011) or undergoing active faulting associated with intraplate deformation. Intraplate deformation is mostly restricted to continental settings, though there are a few exceptions such as the Indian Ocean Basin which is experiencing complex diffuse deformation over a large area (e.g., Bull & Scrutton, 1990) and the south Atlantic near the Rio Grande Rise (Estep et al., 2020; Kardell et al., 2021). At subduction zones, bending of the subducting lithosphere creates a flexural bulge seaward of the trench known as the outer rise. This flexure produces extensional stresses at the top of the plate that are accommodated by the reactivation of faults formed at the spreading center, the creation of new faults, or both (Masson, 1991). Active-source seismic images show pervasive fault systems in the outer rise that can extend well into the upper mantle (e.g., Ranero et al., 2003), which is corroborated by thermomechanical plate bending models (e.g., Faccenda, 2014; Zhou & Lin, 2018). These faults are suggested to act as pathways for fluids to rehydrate the oceanic lithosphere, rejuvenating hydrothermal circulation and causing further precipitation of alteration minerals (Choe & Dyment, 2021; Ivandic et al., 2008). Numerous 2D ocean-bottom seismometer (OBS) reflection/refraction profiles acquired perpendicular to the trench support this theory, as evidenced by reductions in upper mantle P-wave velocities after plate bending that serpentinize the mantle (e.g., Grevemeyer et al., 2007; Ivandic et al., 2008; Shillington et al., 2015). If these low velocity values are exclusively a consequence of serpentinization, then the mantle in some outer-rise systems may contain as much as ∼1.8–3 wt.% H_2O (Shillington et al., 2015). A recent study reveals that these values from trench-perpendicular models could be overestimated if serpentinization is localized along faults, as this creates an anisotropic fabric that must be accounted for (Miller & Lizarralde, 2016). In general, data from widely spaced OBS lack the spatial resolution needed to accurately quantify the amount of water stored in the upper 1–2 km of oceanic crust, which is the primary focus of this study.

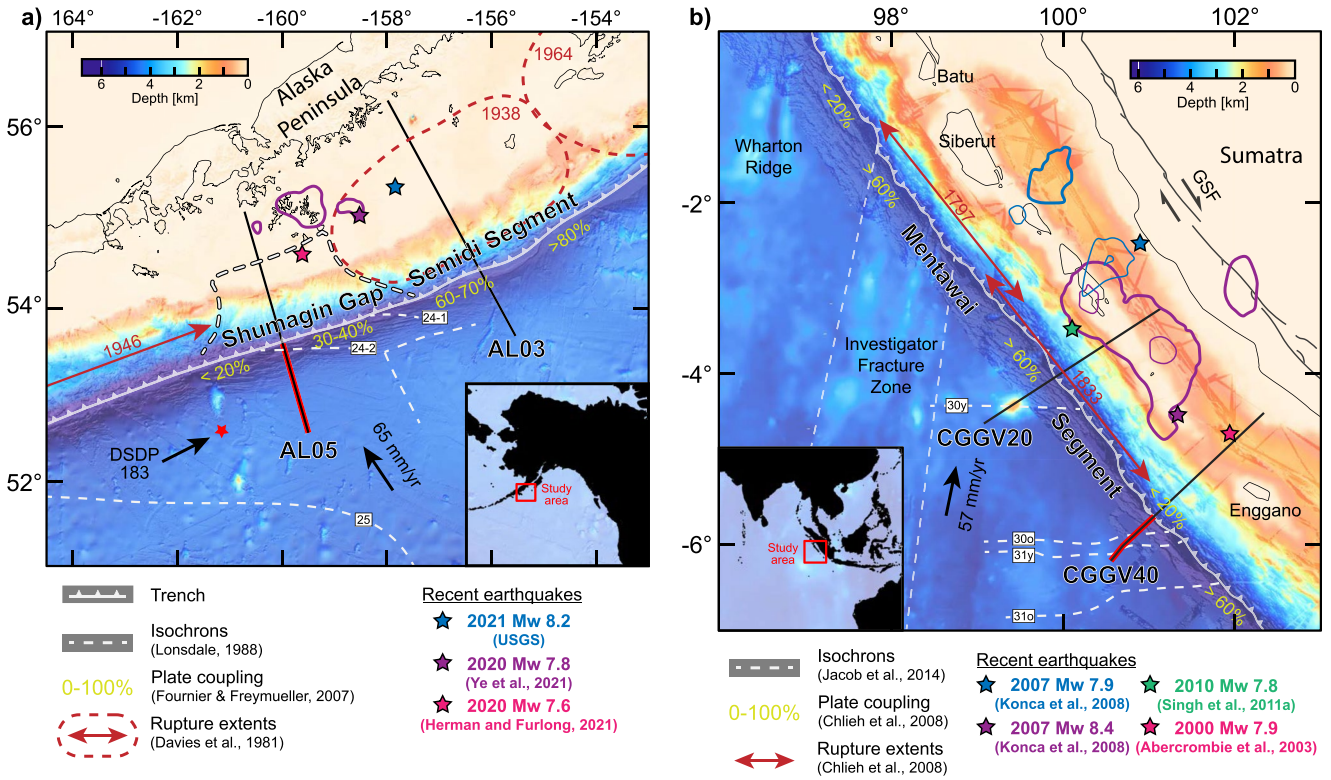

Figure 1. Composite bathymetric maps (GMRT; Ryan et al., 2009) of the two subduction zones with important features labeled. (a) Solid black lines are the same ALEUT profiles showed by Shillington et al. (2015), with the red portion on AL05 denoting our section of interest for this study. Red star is the location of DSDP site 183 from Creager et al. (1973). (b) Same as in (a), but for the second study area offshore Sumatra, Indonesia. Isochrons are from Jacob et al. (2014). MCS profiles are the same as those shown by Singh, Hananto, Mukti, Robinson, et al. (2011) (CGGV40) and by Singh, Hananto, Mukti, Permana, et al. (2011) (CGGV20).

While P-wave velocities are sensitive to altered lithologies in the lower crust and uppermost mantle, crack porosity is believed to account for up to 90% of the velocity variations between in situ measurements and theoretical values for unaltered basalt (Carlson, 2014b). Indeed, the competing effects of fracture porosity, altered lithologies, and presence of free water are difficult to distinguish without the recovery of coincident S-wave velocities, which are more sensitive to fluids. Using densely spaced OBS data, Fujie et al. (2013) produce both P- and S-wave models of subducting oceanic crust, showing elevated P- to S-wave ratios within the upper crust, an observation that suggests the presence of significant amounts of free water. A few other studies have been able to provide constraints on the upper crust (e.g., Canales et al., 2017; Horning et al., 2016); however, there remains a critical lack of porosity and water content estimates for oceanic upper crustal sections prior to subduction.

Recent advancements have been in the processing of multichannel seismic (MCS) data, which are characterized by dense sources and receiver configurations. These include the extrapolation, or downward continuation, of the recorded wavefields to a datum near the seafloor, which have facilitated the recovery of upper crustal velocity structure on the length scales of geologic processes (e.g., 500–1,000 m resolutions; Arnulf et al., 2011). Downward continuation exposes valuable sedimentary and crustal refractions useful for upper crustal travel-time tomography (Berryhill, 1979, 1984; Jimenez-Tejero et al., 2022). Most of the studies employing this method focus on or near spreading ridges (e.g., Arnulf et al., 2011, 2014a; Harding et al., 2016; Henig et al., 2012), with only a few sampling mature oceanic crust (Audhkhasi & Singh, 2019; Kardell et al., 2019). At present, limited information exists on mature upper oceanic crust prior to subduction, and questions remain on the mechanisms behind crustal rehydration near subduction trenches and the amount of water stored in the upper crust before subduction.

In this study, we utilize long (8 km) and ultra-long (15 km) offset MCS data acquired along trench-normal profiles presented by Shillington et al. (2015) and Bécel et al. (2017) offshore the Alaska Peninsula (Figure 1a) and by Singh et al. (2011) offshore South Sumatra (Figure 1b), respectively. Using a combination of downward

continuation and travel-time tomography, we obtain high-resolution models of the upper crustal velocity-depth structure. We then estimate porosity using differential effective medium theory (DEMT) to provide the first ever high-resolution constraints on the water content in old uppermost oceanic crust near two subduction trenches. This paper expands upon previous results by providing an updated perspective on the relationships between deformation style and plate hydration. We use these constraints to speculate on the downdip implications of fluid expulsion at different depths, and specifically how varying amounts of water might modulate the seismogenic behavior both along the megathrust and within the subducting slab.

2. Geological Settings

The study areas, shown in Figure 1, are two of the most seismically active convergent boundaries on Earth: the Alaska Peninsula and south Sumatra subduction zones. Both subduction zones are responsible for some of the largest and most destructive earthquakes recorded in modern history (e.g., Davies et al., 1981; Natawidjaja et al., 2006). Figure 2 shows interpreted 2D prestack time migrated (PSTM; uninterpreted images are shown in Figure S1 in Supporting Information S1) images of both profiles, that exhibit the same broad structural features described here and in previous studies (e.g., Singh, Hananto, Mukti, Robinson, et al., 2011; Shillington et al., 2015; Becel et al., 2017).

2.1. Alaska Subduction Zone

Profile AL05 offshore the Alaska Peninsula lies in the Shumagin Gap segment, just south of the Shumagin Islands (Bécel et al., 2017; Shillington et al., 2015). Here, the 52–56 Myr old, fast-spread (74 mm/yr half rate; Engebretson et al., 1984) oceanic crust belonging to the Pacific Plate subducts nearly orthogonally beneath the North American Plate at ~63 mm/yr (Sella et al., 2002) (Figure 1a). Marine sediments in this region are generally comprised of a Holocene to mid Miocene age pelagic section that rests atop a layer of slowly deposited early Oligocene to late Eocene turbidite beds belonging to the Zodiac Fan (Creager et al., 1973; Li et al., 2018; Stevenson et al., 1983) (Figure 2a).

The Alaska Peninsula subduction zone is divided into segments that exhibit remarkable along-strike variations in plate coupling and seismicity at all depths (Li & Freymueller, 2018; Shillington et al., 2015). Convergence here has been the cause of numerous large and destructive earthquakes, including the 1938 M_w 8.2 earthquake in the Semidi Segment (Johnson & Satake, 1994) and the 1946 M_w 8.6 tsunamigenic earthquake that ruptured the Unimak segment (López & Okal, 2006). Coupling decreases drastically from northeast to southwest, transitioning from full locking in the Kodiak segment to a nearly freely-slipping plate interface in the Sanak segment (Fournier & Freymueller, 2007; Li & Freymueller, 2018). While the Shumagin Gap has not produced a great earthquake ($M_w \geq$ ~8) in at least ~120 years, geodetic data and historical records show the potential for a great earthquake in this area that could be particularly dangerous to coastal communities (Davies et al., 1981). Additionally, a recent series of earthquakes that ruptured the downdip part of the megathrust just adjacent to and within the Shumagin segment are again raising concerns. On 22 July 2020, a M_w 7.8 interplate thrust event ruptured the down-dip part of the eastern Shumagin Gap and was followed a few months later by a M_w 7.6 intraplate strike-slip event ~80 km to the southwest (Crowell & Melgar, 2020; Ye et al., 2021). Stress modeling of these events suggests that they could be related to the difference in coupling between the Shumagin and Semidi segments, in agreement with recent geodetic models (Herman & Furlong, 2021; Li & Freymueller, 2018). More recently in July 2021, a M_w 8.2 interplate event occurred in the Semidi segment that ruptured part of the 1938 M_w 8.2 rupture zone (Ye et al., 2022).

To help constrain the dominant controls on these along-strike variations, Shillington et al. (2015) compared multichannel seismic (MCS) and ocean-bottom seismometer (OBS) wide-angle tomographic models of AL05 and a similar profile, AL03, acquired in the Semidi segment (Figure 1a). They show a correlation between the orientation of the incoming plate spreading fabric with respect to the trench axis and the abundance of bending faults and intermediate-depth seismicity. In the Semidi segment, the incoming plate is heavily sedimented at the outer rise and its pre-existing spreading fabric is oriented oblique to the trench axis, resulting in little bending-related faulting. Conversely, in the Shumagin Gap, the more weakly sedimented incoming plate has a spreading fabric aligned within 10°–25° of the trench, and there is a much greater abundance of bending faults and shallow to intermediate-depth (>50 km) earthquakes (Figure 2a). These observations coincide with a marked

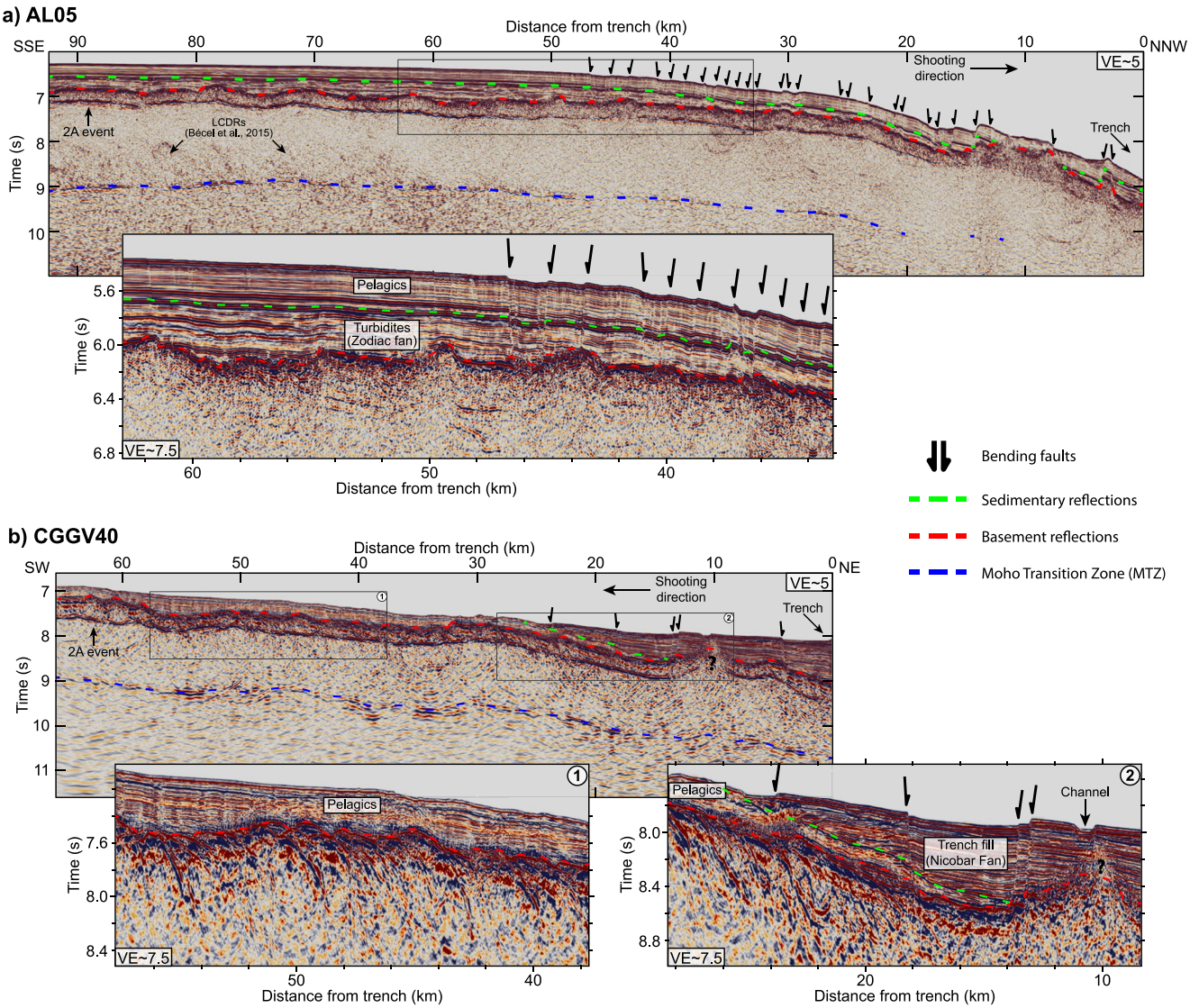

Figure 2. Interpreted reflection images of both profiles. (a) PSTM image of the upper plate along AL05 showing the onset of plate bending toward the subduction trench. The layer 2A event has been merged with the final full PSTM image. The thin black box corresponds to the zoomed inset below. The strong sedimentary reflector delineates the boundary between pelagics and distal turbidites. (b) Same as in (a), but for the over-under processed (Singh et al., 1996) data acquired in the outer rise along CGGV40. The vertical and horizontal scales are the same as in (a). The two numbered black boxes correspond to their respective insets. The green horizon in the second inset represents a boundary between the pelagics and overlying trench fill. Compared to AL05, there are significantly fewer new or reactivated bending faults observed on the more gently dipping upper plate on CGGV40. An uninterpreted version of this figure is shown in Figure S1 in Supporting Information S1.

decrease in upper mantle P-wave velocities on AL05, which was interpreted as due to the presence of a significant amount of water (~1.8 wt.% H_2O) in the form of serpentinite in the upper mantle.

2.2. Sumatra Subduction Zone

Profile CGGV40 samples the incoming Indo-Australian oceanic crust that is 65–68 Myr old and was formed at fast to ultra-fast spreading rates (up to ~90 mm/yr half rate) at the now extinct Wharton spreading center located ~270 km to the northwest of our profile (Jacob et al., 2014) (Figure 1b). This area, called the Wharton Basin, has experienced past and current deformation (e.g., Carton et al., 2014; Singh et al., 2017) largely associated with the collision of India with Eurasia, that is further modulated by the highly oblique subduction of the composite Indo-Australian Plate beneath the Sunda continental plate (Fitch, 1972). Convergence partitions into

dip-slip along the megathrust at about 45 mm/yr and right-lateral strike-slip along the Great Sumatra Fault at 11–28 mm/yr for a bulk rate of 57 mm/yr around 5°S (Bock et al., 2003; Sieh & Natawidjaja, 2000). The inherited spreading fabric inferred from magnetic anomalies makes a ∼40° angle with the trench axis (Jacob et al., 2014). In the outer rise region, the sediment cover is generally thin, as incoming Bengal-Nicobar Fan sediments are blocked by the fossil Investigator fracture zone (IFZ) and Wharton fossil ridge to the north, resulting in thinner, mostly pelagic sediment cover in the outer rise region near the Mentawai Islands to the south. The southward transport of Nicobar Fan sediments along the trench gradually thickens the sediment column to as much as 1 km at the trench (von der Borch et al., 1974; Singh, Hananto, Mukti, Robinson, et al., 2011).

This portion of the Sunda subduction zone has hosted numerous great earthquakes in the past, including the September 2007 M_w 8.4 and M_w 7.9 Mentawai earthquakes (Konca et al., 2008) (Figure 1b). Geodetic and paleogeodetic data that constrain the rupture extents of great earthquakes reveal that the plate interface in the Sumatra region is generally strongly coupled, except for a few segments that appear weakly coupled. These weakly coupled segments coincide with the subduction of topographic features like the IFZ and fossil Wharton spreading center (e.g., Chlieh et al., 2008; Natawidjaja et al., 2006). Additionally, only moderate earthquakes ($M_w < 8$) have occurred in the area south of the rupture patch of the 2007 events. Here, in the vicinity of Enggano Island, Singh, Hananto, Mukti, Robinson, et al. (2011) imaged a 2–4 km high, 40 km wide seamount, at 30–40 km below the forearc basin, using the 15 km-long streamer data acquired on CGGV40 (Figure 1b). The persistence of this feature after more than 160 km of subduction could imply stable sliding, rather than the formation of an asperity, resulting from the dehydration of the hydrothermally altered seamount and accreted sediments (Von Huene & Scholl, 1991). Earthquake relocations show a paucity of seismicity within a ∼50 km radius above and below the seamount suggesting this area is indeed a seismic gap (Singh, Hananto, Mukti, Robinson, et al., 2011). Just seaward of this gap, a M_w 7.9 earthquake occurred in June 2000, consisting of two events, an intraslab strike-slip and interface thrust earthquake (Abercrombie et al., 2003). Geodetic constraints suggest that while segmentation has persisted in this area, megathrust behavior transitioned from partially or fully coupled prior to 2001 to now freely slipping (Chlieh et al., 2008; Prawirodirdjo et al., 2010); however, more recent analyses indicate the presence of shallow frictional locking and a multi-year long slow slip event (Mallick et al., 2021). Thus, the megathrust near Enggano Island could pose a greater seismogenic risk than previously thought.

2.3. Seismic Data

The Sumatra dataset was acquired in 2009 aboard the CGGVeritas seismic vessel *Geowave Champion*, towing one 15 km-long streamer, the longest ever used at the time, and two 6 km-long streamers in an over/under configuration (Singh et al., 1996). The seismic source was a large 9,600 in^3 48-element airgun array. Unlike conventional MCS surveys, the source and longest streamer were towed deeper at 15 and 22.5 m, respectively, to increase the recovery of low frequencies down to 5 Hz; two shorter streamers were towed at 15 and 7.5 m. The streamers were solid-state rather than fluid filled, which reduces noise and decreases the minimum recovered frequency down to 2 Hz. The shot interval was 50 m and the record length was 20 s.

The Alaska dataset was acquired in 2011 aboard the R/V *Marcus G. Langseth* using two 636-channel, 8 km-long fluid-filled streamers and a 6,600 in^3, 36-element airgun array. The source was towed at 12 m and the two streamers were towed at 9 and 12 m depth, respectively, to enhance the recovery of lower frequencies as much as possible. The shot interval was 62.5 m and the record length was 22.5 s. The receiver group spacing for both datasets was 12.5 m. In our study, we only use the data from the streamer towed at a 12 m depth.

3. Methods

To unravel upper crustal seismic arrivals, and improve the resolution in the upper oceanic crust through a better distribution of turning rays, we employ downward continuation of the seismic wavefield (e.g., Arnulf et al., 2011; Audhkhasi & Singh, 2019; Jimenez-Tejero et al., 2022; Kardell et al., 2019). We utilize an efficient downward continuation method based on the Kirchhoff integral theorem (Berryhill, 1979) that has been successfully adapted to operate on prestack data (Arnulf et al., 2011; Berryhill, 1984; Jimenez-Tejero et al., 2022). Downward continuation allows us to bypass most of the water layer by extrapolating the data recorded near the sea surface to a datum closer to the seafloor. First, the receiver wavefields of the common-shot data are extrapolated to 75 m

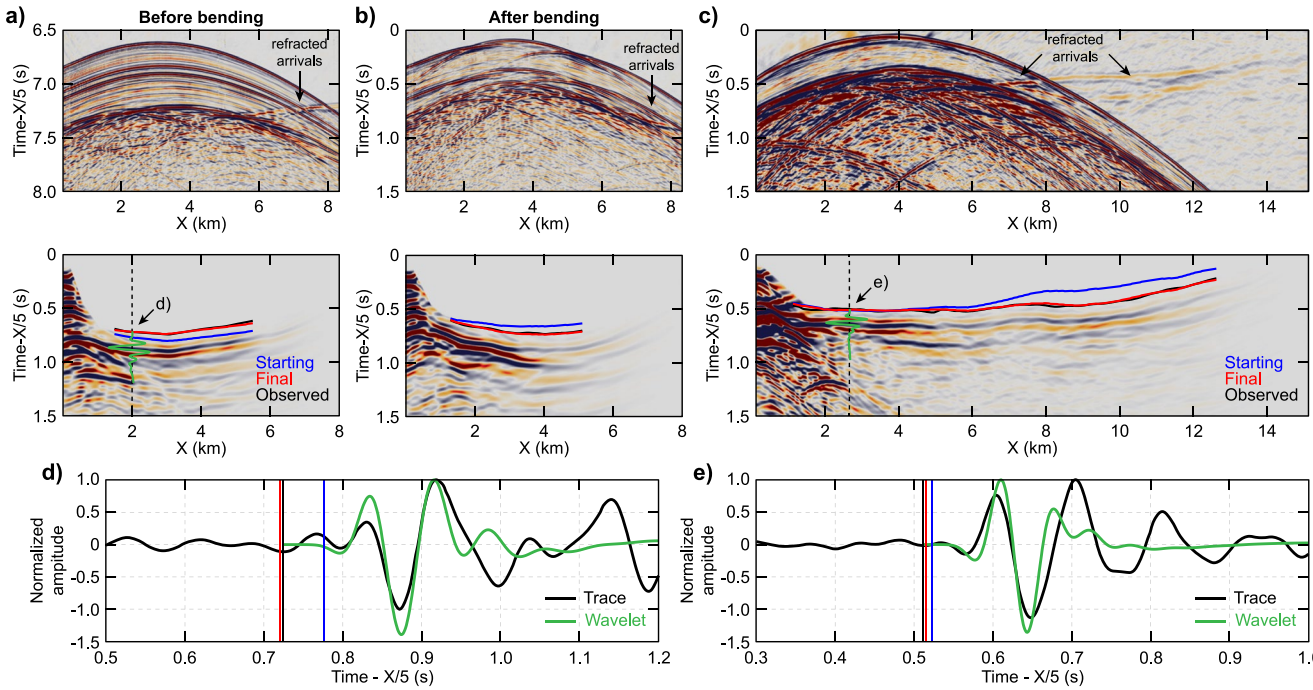

Figure 3. Example shot gathers before and after downward continuation. (a) Shot gather 4997 acquired outside the bending area on AL05 before (top) and after (bottom) downward continuation. Modeled Travel times are shown as colored lines. (b)-(c) same as in (a) but for shot 4291 on AL05 in the bending area (b) and shot 1699 on CGGV40 (c) across the low velocity anomaly. Streamer locations for each shot gather are plotted in Figures 4a and 5a. Extrapolation reveals more than twice the offset of first-arrival refractions seen in the surface gathers. (d)-(e) Seismic traces plotted with the identically filtered (i.e., identically shifted) wavelet starting at the observed travel time. Respective locations are marked on the bottom panels of (a) and (c). The waveforms of the filtered wavelets match well with the refracted arrivals.

above the seafloor. Reciprocity allows us to then extrapolate the source wavefields to 75 m above the seafloor by applying the same operation in the common-receiver gather domain. Extrapolation both improves the imaging conditions by collapsing diffracted energy while also moving near-offset refracted arrivals ahead of the seafloor reflection (Figure 3).

3.1. Pre-Processing and Downward Continuation

Before applying the downward continuation method, some pre-processing is required. This includes removing high-amplitude noise from the data and accounting for noisy or weak channels, since strong amplitude variations can produce migration artifacts during extrapolation. It is important to preserve the original low-frequency amplitude and phase information. Hence, we apply minimal pre-processing to the data to remove only the strongest noise. Swell noise was reduced using a combination of iterative FX (frequency-offset) filtering within the 0–10 Hz band, specifically designed to conserve the lowest frequency signals down to 2 Hz for CGGV40 and 3 Hz for AL05. For the AL05 data, we also identify and interpolate very weak or noisy channels, and balance trace amplitudes across the entire dataset to preserve continuity of the seismic wavefield. The CGGV40 data do not contain any persistent bad traces and have a much higher signal-to-noise ratio, so trace interpolation and balancing were not necessary. Then, we applied a predictive deconvolution to minimize the source ringing effect, which is particularly strong for CGGV40 due to the larger, deep-towed source. The pre-processed data were then used to produce stacked sections where a seafloor horizon could be picked to define the extrapolation datum. The seafloor horizons were then converted to depth using the average water velocities and smoothed to avoid producing discontinuities associated with sharp changes in seafloor topography.

The source and receiver wavefields were extrapolated to a conformal datum located 75 m (~100 ms) above the seafloor horizon. We apply sixth-order Butterworth band-pass filters between 2 and 20 Hz for CGGV40 and 3–15 Hz for AL05 before the first extrapolation step and similar low-pass filters at 20 and 15 Hz prior to the second step to prevent aliasing and further remove unwanted noise. Additionally, we taper the edges of each gather at each step to minimize edge effects. After extrapolation, we update the initial seafloor profiles by

comparing estimates of the seafloor reflection arrivals with travel times picked on the first trace of each extrapolated gather. Seafloor travel times are found by cross-correlating an identically filtered, data-derived source wavelet with each first-offset trace and calculating the maximum lag between the two (e.g., Harding et al., 2016). We use the method of Collier and Singh (1997) to extract source wavelets by averaging seafloor reflections on the nearest offset traces of multiple shot gathers in areas of flattest seafloor. The modeled seafloor is then corrected by converting travel-time differences to depth using the average water velocity and the data are re-extrapolated.

3.2. Tomography Method

We use the iterative tomography algorithm of Arnulf, Harding, Kent, et al. (2014) who developed an updated version of the tomography code of Van Avendonk et al. (2004) that is more suitable for a downward continuation geometry. We picked travel times every two shots for AL05 (125 m spacing) and every three shots for CGGV40 (150 m spacing) to sample at least twice within the first Fresnel zone at the seafloor (Henig et al., 2012). We used a semi-automatic cross-correlation technique to pick a total of 186,096 arrivals on AL05 and 324,900 arrivals on CGGV40. Figure 3 shows shot gathers before and after extrapolation for both profiles, with their respective observed and modeled travel-time data overlain. Depending on the water depth and sediment thickness, we gain as much as 6 and 10 km of offset useable for inversion for AL05 and CGGV40, respectively, after downward continuation. Because the true first arrival is often distorted by noise and difficult to interpret, we pick on the second zero crossing of the refracted events The apparent travel times are further delayed by the high-order band-pass filters applied during the extrapolation. Thus, to avoid calculating erroneously slow velocities (i.e., erroneously high porosities), we shift each pick by the time of the same crossing on the identically filtered (i.e., identically shifted) source wavelets (Figures 3d and 3e). Because downward continuation moves energy closer to the source and smears data at the farthest offsets, we remove picks at offsets greater than ∼5.5 km for AL05 and ∼12.5 km for CGGV40. Additionally, we exclude any picks arriving after the forward modeled seafloor reflection times for each shot gather to help ensure that only true first arrivals were picked.

Since only turning rays in the crust are considered here, it is necessary to incorporate a fixed sediment layer (i.e., not updated during inversion) and basement interface during the inversion as our main goal is to derive the most accurate velocities for the upper oceanic crust. For AL05, two different velocity-depth gradients were used for the sediments: one above and one below the strong sedimentary reflection that marks the transition from pelagic sediments to distal turbidites (Figure 2a). Velocity-depth gradients were taken from velocity measurement of sedimentary rocks from DSDP Site 183 (Creager et al., 1973) just southwest of the profile (Figure 1). For CGGV40, in the absence of velocity constraints from drilling, we use a single velocity gradient layer that was derived by laterally smoothing root mean square (RMS) velocities used to migrate the data in the prestack domain. RMS velocities were then converted to interval velocities to create the sediment layer and to convert the basement horizons into depth. For the crust, starting models were created by hanging a smoothed version of the average crustal structure for fast-spread, mature oceanic crust presented by Christeson et al. (2019) below the sediment-basement interface. The initial crustal models were then flattened by the basement horizon and smoothed in slowness using a 250 m Gaussian filter before being un-flattened.

3.3. Inversion Strategy

We performed iterative regularized inversions in a damped least squares sense, minimizing a cost function that incorporates both the data misfit and model roughness (Van Avendonk et al., 2004). Before each inversion, travel times were forward modeled using a combination of the shortest path z ray bending methods grid (Moser, 1991; Figures S2 and S3 in Supporting Information S1). The graphing grid used for ray tracing was spaced 12.5 m in both directions and the inversion grid was discretized at 25 m vertically and 150 m horizontally for both profiles. The roughness matrix penalizes both the first (gradient) and second (curvature) derivatives of the model update, rather than just the model perturbation, in order to help obviate the influence of the starting model on the final result. We set horizontal derivative smoothing weights to be six times greater than vertical to maximize the recovery of the strong vertical velocity gradients expected in upper oceanic crust. At each step, we aimed for a Chi-square reduction of ∼30–40%, which was facilitated by applying the secant method to vary regularization values (Van Avendonk et al., 1998), until a Chi-square of ∼1 was reached, indicating the travel-time errors lie within the prescribed uncertainties (10–14 ms).

The misfit after each iteration is determined by the Chi-square, which is the sum of the squared travel-time residuals weighted by their respective pick uncertainties. We estimate overall uncertainty as the root sum of the

squares of the individual uncertainties associated with the average travel-time difference between the original and the smoothed seafloor horizons (~5 ms); variations in the source and receiver depths (~2 ms); the forward modeling of refractions (~5 ms) (e.g., Moser, 1991); the downward continuation method (~5 ms); and picking travel times (~4 ms) for a total of 10 ms. For AL05, we assigned a slightly higher travel-time uncertainty of ~14 ms since the data have a lower signal-to-noise ratio and required more extensive pre-processing prior to downward continuation.

3.4. Model Resolution

One measure of the density of seismic rays is the derivative weight sum, or DWS, which provides a relative measure of nodal samplings in the model space (Figure S4 in Supporting Information S1). Elevated DWS values are reasonable indicators of good model resolution, but often misrepresent the actual resolvability, especially where values are low (Zhang & Thurber, 2007). Several tests were performed to further examine the ability of our inversion scheme to recover positive and negative velocity anomalies of various sizes and to produce consistent results regardless of the starting model used. Checkerboard tests were performed for 10% sinusoidal anomalies sized 7.5 × 1.5 km and 5 × 1 km (Figures S5 and S6 in Supporting Information S1). These perturbations were added to the final tomographic models, which were then used to forward model synthetic travel-time picks. Next, the same inversion scheme was applied, starting from the same initial models, until the Chi-square values were reduced to ~1. For both models, anomalies sized 7.5 × 1.5 km are recoverable at all depths and the 5 × 1 km anomalies are recovered in the upper ~1 km of the crust. Because we opt for a larger ratio (6) of horizontal to vertical weights, smaller anomalies are not recovered. While reducing the ratio of these weights to 2 allows for their partial recovery, this comes at the expense of not being able to fit the nearest and farthest offset travel times and produce the strong vertical velocity gradients expected in the upper crust. Finally, we performed inversions using the same travel-time picks and inversion parameters, but for a less realistic starting model consisting of a single gradient in the crust. Figure S7 in Supporting Information S1 shows that nearly identical results are produced regardless of the chosen starting model, with final models differing on average by no more than 50 m/s for CGGV40 and 50–100 m/s for AL05. The strong smoothing accomplished by regularization essentially removes any dependency on the starting model in the areas where ray coverage is dense. Lastly, we tested the effect of varying the sediment velocities while ensuring the same thickness in time for the fixed sediment layer. Figure S8 in Supporting Information S1 shows nearly identical results obtained using two different starting models where the sediment velocities were perturbed by ±10% from the original starting model.

3.5. Reflection Imaging and Layer 2A

To provide additional information on the sediment and crustal structures, we used a processing flow that incorporates constraints from our tomography results during PSTM instead of relying on conventional velocity analysis (Figure 2). For AL05, we used the same pre-processed data previously used for downward continuation. For CGGV40, we used pre-processed gathers courtesy of CGG that combined information from all three of the streamers for a more broadband response (e.g., Singh et al., 1996). Before migration, we designed parabolic Radon filters every 100 CMPs to attenuate internal multiples in the crust for both datasets. We then converted the final two-layer tomographic models to RMS velocity in time and smoothed in slowness by a 250 m wide 2D Gaussian filter. The same migration aperture, 10 km wide, was used starting ~1 s above the seafloor to better image steep reflectors and collapse diffractions in the upper crust.

To image the layer 2A event, we followed the method of Harding et al. (1993) and picked stacking velocities every 50 CMPs (~300 m) that best flatten the retrograde branch of the triplication (Figures S9 and 10 in Supporting Information S1). We supply a constant stacking velocity for each CMP and interactively pick top and bottom mutes to isolate the 2A event on moveout-corrected gathers. After stacking, we apply a poststack time migration using the same constant stacking velocities. We then apply a mute to remove any unwanted migration artifacts followed by a coherency filter to suppress noise. The PSTM sections in Figure 2 have been merged with the migrated 2A event to create composite images. For display purposes, the average amplitudes of the 2A event have been scaled to match the average amplitudes of the basement reflection. We interpret the layer 2A horizon in TWTT as the first arrival of the stacked event on the merged PSTM images and then convert it to depth using the velocities from our final tomography results. The 2A pseudo-reflections stack in at a range of velocities and their subsequent depths are subject to a certain degree of uncertainty (e.g., Audhkhasi & Singh, 2019). To remove potential

bias due to short wavelength variations that cannot be resolved by stacking the 2A event with sparse velocities, and to facilitate comparison with other studies, we assume a single layer 2A thickness for the entire profile. This is calculated by taking the mean of the difference between the depth-converted 2A horizon and the fixed basement interface. A 5% perturbation in either direction to the stacking velocities used to image layer 2A results in less continuous 2A events that are more difficult to interpret, with average deviations from our preferred horizons of ∼75 m for AL05 and ∼71 m for CGGV40 (Figures S9 and 10 in Supporting Information S1).

4. Results

4.1. Structure Inferred From Reflection Images

Our PSTM results provide an unprecedented, high-resolution view of the sediments and upper crustal structure along both lines (Figure 2). The seafloor and basement depth horizons, which were held fixed during the inversions, match well with those in the stacked sections after being converted back to time. Therefore, we use these horizons to interpret sediment thicknesses, basement structure, and fault throws.

4.1.1. Sediment and Basement Structure Offshore Alaska

AL05 encompasses the transition into the outer rise around 45–55 km from the trench, where previously flat oceanic lithosphere gradually begins to bend to as much as 3–4° calculated at the top of the crust (Figure 2a). Prior to significant bending (>50 km from the trench), the basement topography is smooth and undulatory at wavelengths ranging from 2 to 18 km with small vertical variations (<∼300 m). Prior to bending, the bulk sediment cover is thicker than that approaching the trench, with an average of ∼500 m; few to no faults are observed in the sediments and crust. While the upper pelagic layer maintains a thickness around 230 m across the entire profile, the lower layer of distal turbidites from the Zodiac Fan exhibits much more variation (e.g., Stevenson et al., 1983) and gradually thins toward the trench with an average thickness of ∼125 m. This thinning also coincides with the appearance of a dense network of bending related faults spaced 0.5–2 km apart, as illustrated by the inset in Figure 2a, with throws up to ∼250 m at the basement.

The uppermost oceanic crust is largely void of coherent reflections except for the merged layer 2A event (Figure 2a). The Layer 2A event, corresponding to a high-amplitude retrograde arrival, is generally visible between 4 and 6 km offset in the surface gathers (Figure S9 in Supporting Information S1), and stacks in at most distances until ∼17 km from the trench before disappearing. The resulting horizon approximately mirrors the basement topography with an average thickness of ∼250 ms (or ∼540 m) where visible. We image the same lower crustal dipping reflections (LCDRs) around 60–90 km from the trench, as observed by Bécel et al. (2015); these LCDRs do not pass through the reflective Moho or extend upwards into the crust. Between 20 and 40 km distance range, there is some faint reflectivity in the upper and lower crust that is similar in dip and crustal depth to the LCDRs, located just beneath some of the larger and more clustered bending faults. These reflections are not obviously associated with the bending faults above, and there is no evidence that they offset the Moho. Moho reflections vary across the entire profile, though most notably in the bending area where amplitudes are generally reduced compared to those seen before bending. Within ∼50 km from the trench, the Moho appears intermittently, producing a very weak signal beneath areas where some of the largest bending faults are observed before disappearing almost entirely within ∼20 km from the trench.

4.1.2. Sediment and Basement Structure Offshore Sumatra

CGGV40 lies entirely within the bending area. Here, the crust dips gently toward the trench at ∼0.8° until around 33 km from the trench where the dip increases to as much as ∼1.8° as it approaches the trench (around half as much as the maximum dip on AL05). Basement relief varies up to ∼130 m over 5–10 km distances assuming relative deviations from a smoothed fit to the basement (Figure 2b). At distances greater than 25 km from the trench, a thin veneer of 100–350 m thick, weakly reflective pelagic sediments blankets the crust. Here, we observe a combination of sparse steeply dipping faults with small throws (10–50 m) and undulations that correspond to short wavelength (0.5–1 km) variations in the basement topography. Closer to the trench axis, this layer begins to thin rapidly before terminating below a progressively thickening sequence of more reflective trench infill that reaches ∼800 m in thickness. The unconformity between these two sedimentary sections creates a strong reflection that coincides with the steepening of the subducting plate and the initiation of faulting. These seaward dipping normal faults are less abundant than in Alaska and, like those imaged by Singh, Hananto, Mukti, Permana, et al. (2011) on profile

CGGV20 (Figure 1b), are irregularly spaced 0.4–8 km apart with fault throws that reduce up-section. We observe basement throws between 50 and 110 m, which are considerably smaller than those seen to the north (300–400 m). The basement reflection is sharp and well imaged, except for a ~6 km wide area about 11 km from the trench where we observe a basement high. Reflectivity at and below the basement (and down to the Moho) in this area appears significantly distorted by high-frequency artifacts, that could be related to the sampling of out of plane energy. Moreover, this is the only area where the 2A event is not well resolved (Figure 2b); the associated retrograde arrivals appear in nearly all the surface gathers at offsets between 5 and 8 km (Figure S10 in Supporting Information S1), and stack in on average ~290 ms (or ~640 m) below the basement horizon.

The oceanic crust is highly reflective throughout the entire section and is characterized by the presence of numerous seaward and trenchward-dipping reflections that cross through most of the oceanic crust and even into the uppermost mantle. Most of these arrivals cannot be definitively linked with disruptions at the basement interface, however, some of these dipping reflections appear to cross through the Moho discontinuity (without clearly offsetting it) and extend deep into the upper mantle (e.g., ~50 km from the trench; Figure 2b). The Moho is well imaged everywhere but varies drastically in amplitude and style of reflectivity. In some areas, this event is a single sharp reflection, as is the case on AL05; however, in other areas (e.g., ~40 km from the trench), we observe a more banded style of reflectivity.

4.2. Velocity Models, Porosity and Water Content

Figures 4 and 5 show the final inverted models, their corresponding velocity anomalies (obtained by subtracting the starting model), and the total gradient magnitudes for AL05 and CGGV40, respectively. Travel-time residuals

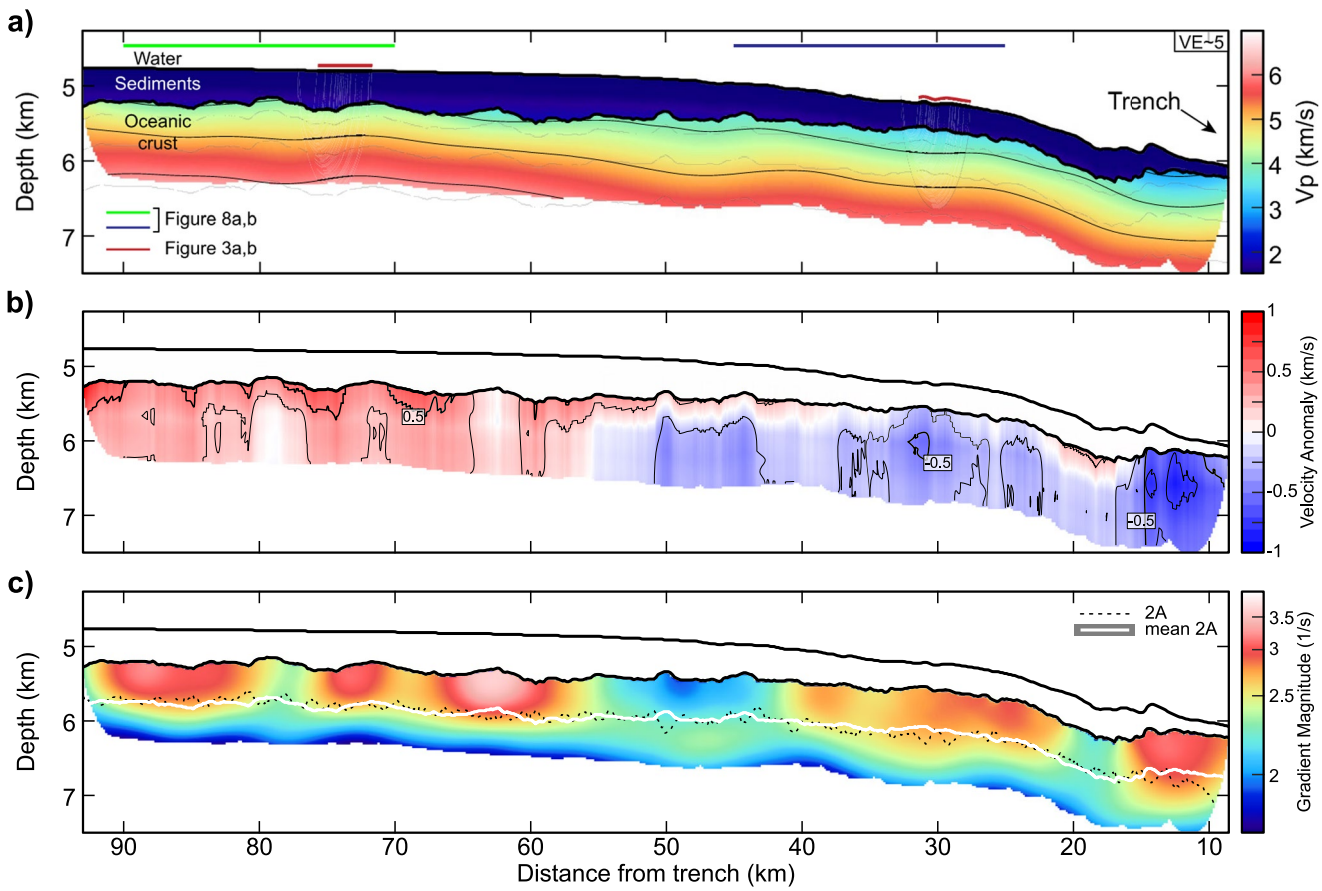

Figure 4. Tomography results for AL05. (a) Preferred final model after 11 iterations of travel-time inversion (Chi-square of 1.02). Thick solid black lines are the seafloor and basement horizons fixed during inversion. Solid thin lines are 1 km/s velocity interval contours from 3 to 6 km/s. The data are masked by the DWS, which has non-zero values down to ~1.2 km below the basement on average. (b) Velocity anomaly calculated by subtracting the starting model from the final model. Velocity contours are plotted from −1 to 1 km/s with a 0.25 km/s interval. (c) Total velocity gradient magnitude in the upper crust calculated from (a). Dotted black line is the depth converted 2A event horizon and the solid white line is the mean depth of the 2A.

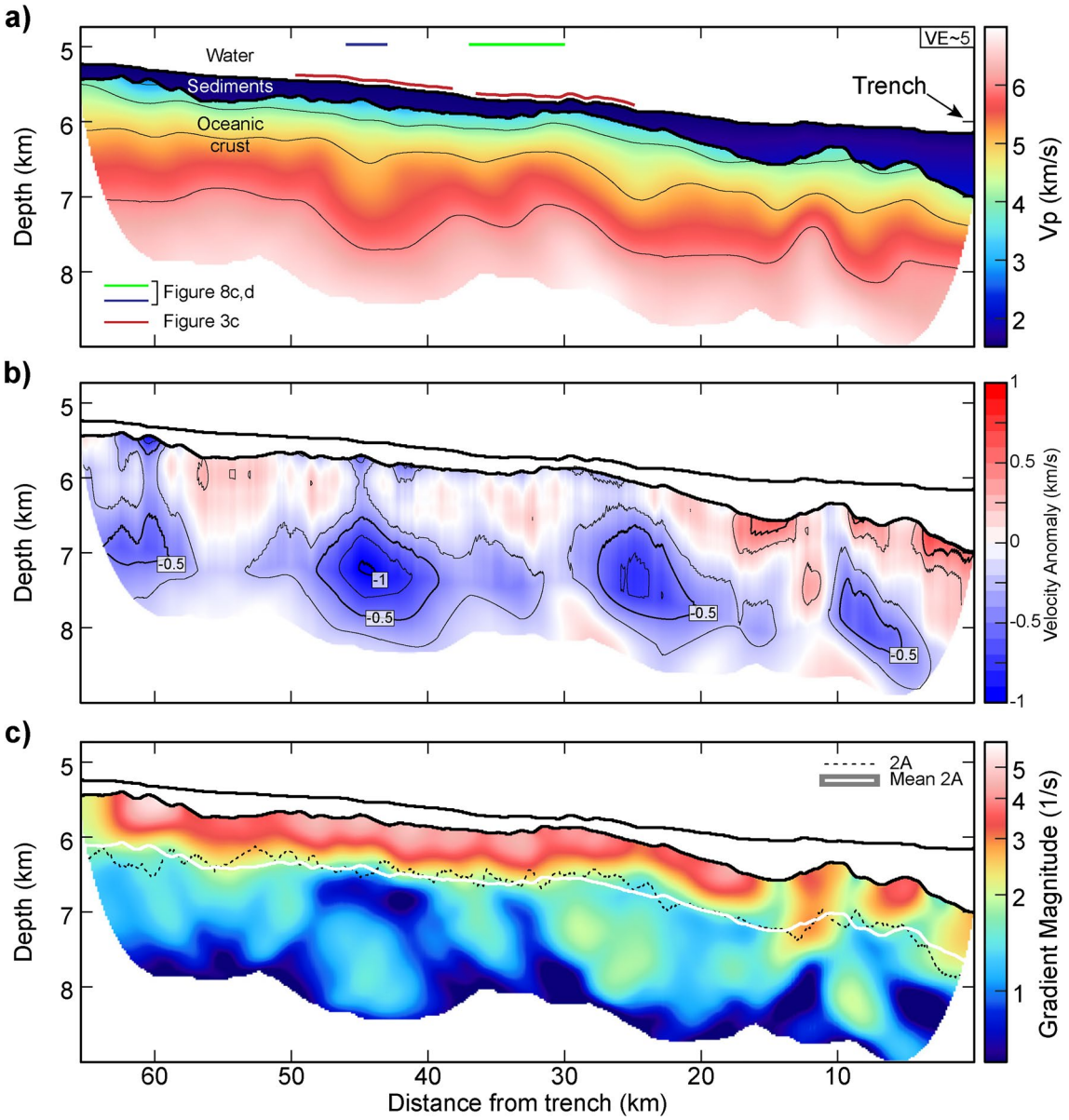

Figure 5. Same as in Figure 4, but for the CGGV40 after 10 iterations of travel-time tomography (Chi-square of 0.95). The longer streamer allows for sensitivity down to ~2.3 km below the basement.

for both final models are plotted as a function of receiver location and time as well as source location with streamer offset in Figure 6 and show a good fit to the data at nearly all distances. The deepest ray penetration is down to ~1.2 km below the basement along profile AL05 and ~2.4 km along CGGV40 as a result of incorporating more than twice as much source-receiver offset during inversion (Figure 3). The ray coverage is dense across both profiles (Figure S4 in Supporting Information S1), except for a few small areas (e.g., ~15 and ~10 km from the trench on AL05 and CGGV40, respectively). The average layer 2A thickness is 540 m on AL05 and 640 m on CGGV40, and these values agree well with the depth of the transition zone recovered on IODP site 1256D (Figures 7a and 7b; Carlson, 2014a). Both models appear to recover the high vertical velocity gradient in the uppermost crust. The transition to a lower gradient in the upper crust agrees very well with the depth converted 2A/B horizon (Figures 4c and 5c), although the effect is less apparent on AL05. The velocity structure along CGGV40 varies more in all directions compared to AL05. Although more extensive pre-processing was needed

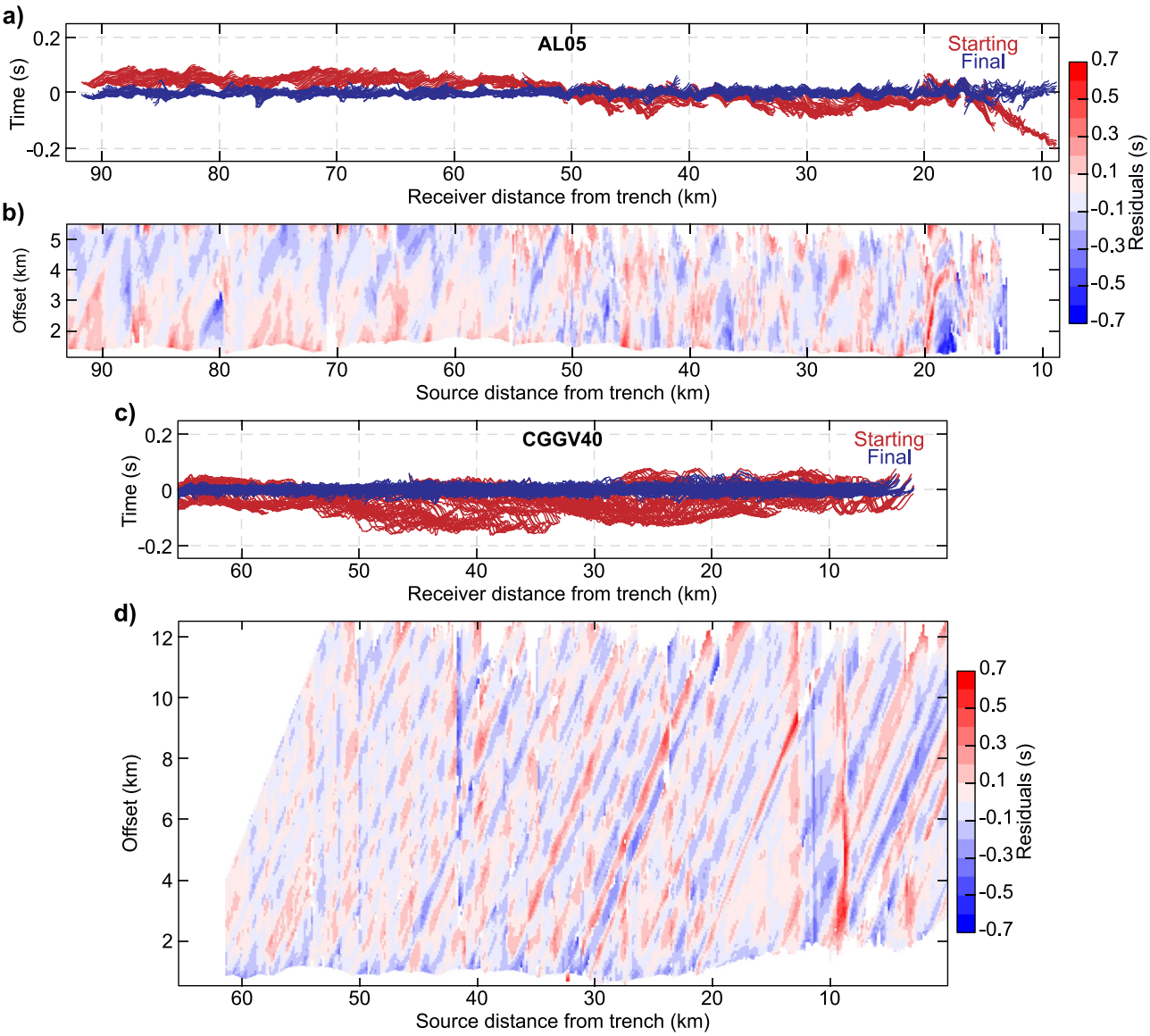

Figure 6. Travel-time residuals for both inversions. (a) Starting (red) and final (blue) travel-time residuals for AL05 as a function of receiver location. Positive residuals indicate the starting model is too slow >50 km from, and negative residuals suggest it is too fast within 50 km of the trench. (b) Final residuals for AL05 as a function of source distance from the trench and receiver offset. (c)-(d) Same as in (a) and (b), but for CGGV40. Receiver offset gradually decreases toward the end of the line as data were omitted where the vessel was turning.

for AL05 and greater pick uncertainty was assigned, the difference in levels of heterogeneity inferred in both crusts is likely to be real.

To estimate the amount of porosity from the velocities inferred from the streamer tomography, we use a DEMT scheme of Taylor and Singh (2002). We calculate velocity-porosity relationships in the same way as Audhkhasi and Singh (2019) for inverse crack aspect ratios between 5 and 50 and infer a basalt lithology with saturated pores for the entirety of both models (Figure 7). To avoid overestimating the total amount of water in the crust, we calculated the elastic parameters needed for DEMT assuming a zero-porosity altered basalt with a P-wave velocity of 6.74 km/s (containing ~2 wt.% of structural water; Carlson, 2014b, which is significantly less than the highest measured values around 7 km/s for unaltered basalt (Wilkens et al., 1991). The density is taken to be 2,930 kg/m^3 (Carlson, 2014a), and the corresponding S-wave velocity is 3.89 km/s assuming a Poisson's ratio of 0.25, as reported by Collier and Singh (1998). For seawater filling the pores, we assumed a P-wave velocity of 1.515 km/s (the same used for downward continuation), S-wave velocity of 0 km/s, and density of 1,030 kg/m^3.

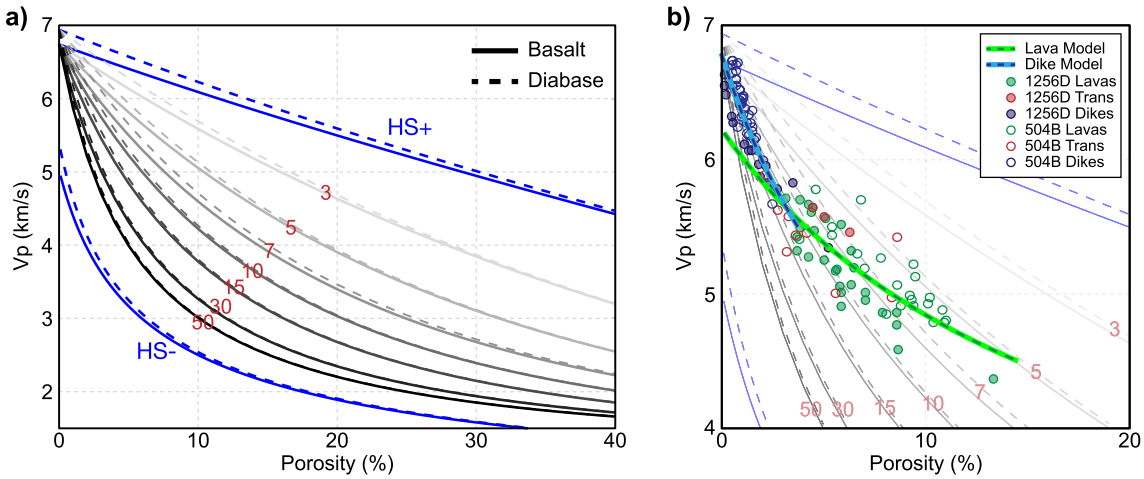

Figure 7. Porosity estimation method. (a) Velocity-porosity relationships calculated using a DEMT for basalt (solid lines) and diabase (dashed lines) host materials filled with seawater for different inverse aspect ratios between 3 and 50 labeled in red. The blue lines are the Hashin-Shtrikman upper (+) and lower (−) bounds. (b) Zoom in of the curves in (a) from 0% to 20% porosity along with borehole measurements of velocity and apparent porosity for the lava, transition zone, and dike sections from sites 1256D and 504B (Carlson, 2010). Solid green and blue lines are the best fitting models from Carlson (2014a) for the lavas and dikes, respectively. For mature oceanic crust, inverse aspect ratios between 5 and 15 for the lavas and 10–30 for the dikes best explain the borehole data.

The relationships calculated via DEMT were then used to produce porosity models for each inverse aspect ratio, which were then converted to wt.% H_2O. Figure 8 shows relative velocity probability plots as well as porosity and wt.% H_2O assuming an inverse crack aspect ratio of 10 computed at each depth below the basement interface for both profiles. While lower inverse crack aspect ratios (5–7) might explain some of the values measured in the lavas at site 1256D, we choose a value of 10, as it is necessary to account for the fact that in situ porosity measurements of basalt do not capture the additional, large-scale porosity features associated with fractures and abyssal hill faulting that have a strong impact on seismic velocity (Carlson, 2014b). Table 1 summarizes our estimates of upper crustal pore water as well as the limited estimates made, both before and after bending, for studies focusing on subduction zones. Water content was recalculated from porosity values using the same elastic parameters specified for DEMT.

4.2.1. Upper Crustal Velocity, Porosity, and Water Content Estimates Offshore Alaska

Sediment velocities offshore Alaska are constrained by the values measured at DSDP site 183 (Creager at al., 1973) (Figure 1). The same two sedimentary units that we fixed during inversion were recovered in the borehole data. In our model, velocities reach an average of 1.6 km/s at the high-amplitude sedimentary reflector that represents the boundary between the pelagic and turbidite sediments and increase to an average of ∼1.95 km/s at the base of the sedimentary layers.

Within the upper oceanic crust, the most striking feature is the marked decrease in velocities at all depths that begins with the onset of bending related faulting (Figure 4a). This negative velocity anomaly (Figure 4b) is evidenced by the change in shape of the extrapolated gathers (Figures 3a and 3b) and the shift in initial travel-time residuals from mostly positive to negative values toward the trench (Figure 6a). The 1D velocity and porosity plots (Figure 8a) show an approximately bimodal distribution before and after bending that closely mirrors where reduced P-wave velocities in the upper mantle were observed by Shillington et al. (2015) along the same profile. Prior to bending, between 70 and 90 km from the trench, velocities average 4 km/s at the top of layer 2A, 5.2 km/s at the base of 2A, and approach 6.4 km/s at the depth limit of resolution. In the bending area, averaged between 25 and 45 km from the trench, these values are reduced to 3.5 km/s, 4.6 km/s, and 6.2 km/s, respectively. This corresponds to an increase in average porosity before and after bending from 8.0% to 11%%, equivalent to 2.8 to 3.9 wt.% H_2O, for 540 m of subducting basalt (i.e., layer 2A) or from 4.8% to 7.1%, equivalent to 1.7 to 2.6 wt.% H_2O, for 1.15 km of subducting basalt (i.e., full model thickness before bending) (Table 1).

From ∼40 to 55 km, where velocities begin to decrease, the vertical velocity gradients decrease from values as high as 4 s^{-1} to values as low as 1 s^{-1}. The amplitude of the layer 2A event is also considerably reduced in this

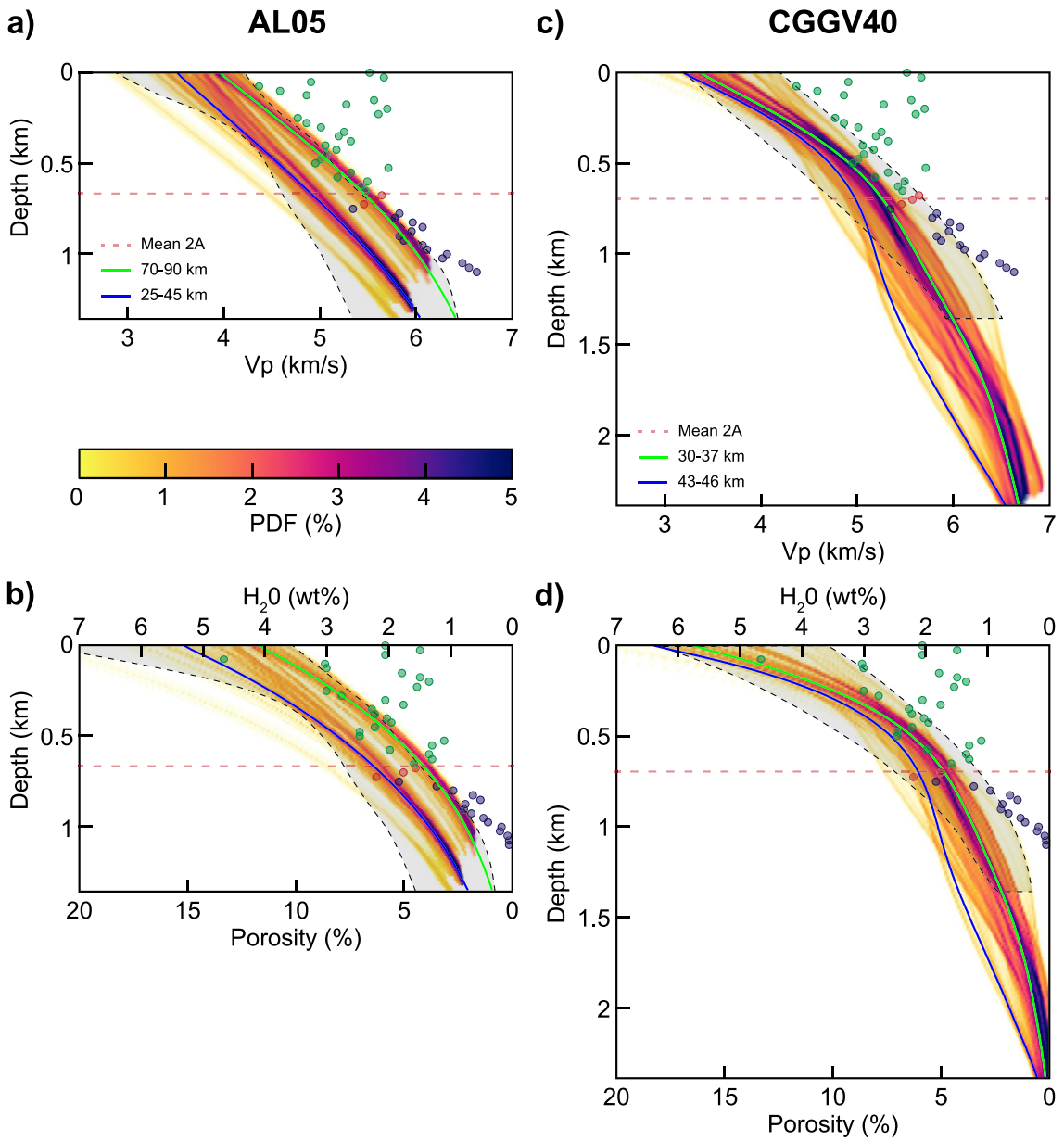

Figure 8. Relative probability estimates for velocity and porosity calculated at each grid point below the basement within the area of ray coverage (i.e., DWS >0) using bin widths of 10 m/s and 0.05% porosity. (a) Green, red, and blue dots are the same as those in Figure 7b from site 1256D (Carlson, 2014a). Red dashed line is the average thickness of layer 2A. Blue and green lines are the average velocities below the basement between 25 and 45 km (bending area) and 70–90 km (outside bending area) from the trench, respectively. Shaded region bound by dashed lines are the velocity bounds from CGGV40 for comparison. (b) Same as in (a), but for porosities calculated using DEMT assuming an inverse aspect ratio of 10 and a basalt lithology. The upper axis shows the corresponding value for wt.% of free water (c)-(d) Same as in (a) and (b) but for CGGV40. Blue and green lines are the averaged velocities and porosities between 43 and 46 km (low velocity anomaly) and 30–37 km, respectively.

region. A similar deviation occurs in a 5 km area around 20 km from the trench, but with velocities in layer 2A that are higher than the surrounding values. This occurrence corresponds to a decrease in both time and depth of the 2A horizon with respect to the basement. Apart from this area, the general trend of decreasing velocities toward the trench is maintained throughout the bending area. Within ~15 km from the trench, we observe vertical gradients greater than 3 s^{-1} and velocities as low as 3 km/s below the largest observed bending faults; however, the data quality in the region rapidly deteriorates and the area is subject to greater dependence on the starting model (Figure S7 in Supporting Information S1). Checkerboard tests suggest that at least the upper ~500 m in this area

Table 1
Summary of Water Content Estimates From Studies of the Incoming Plate

	Water content estimates (wt.% H_2O)							
	Before bending				After bending			
	2A		2B		2A		2B	
Setting	**struct.**	**pore**	**struct.**	**pore**	**struct.**	**pore**	**struct.**	**pore**
Global averages and drill cores	2[a]	-	2[a]	-	2[a]	-	2[a]	-
	2–3[b]		0.5–2[b]					
			1–3[c]					
AL05	-	2.8	-	-	-	3.9	-	-
CGGV40	-	-	-	-	-	3.2	-	0.8,1.3
Nicaragua (Naif et al., 2015)	-	2.6–4.3	-	0.9	-	3.0–4.8	-	1.6
Cascadia (Canales et al., 2017)	-	-	-	0.5–2.1	1.7–1.9	2.8–3.2	0.3	2.3–2.4

[a]Global averages are from Peacock (1990). [b]Estimates from drill cores are from Rüpke et al. (2004). [c]Estimates from drill cores are from Carlson (2003).

is well resolved (Figure S5 in Supporting Information S1), suggesting an average porosity of 10%, or 3.2 wt.% H_2O, with values as high as 20%, or 7 wt.% H_2O in the uppermost 1.15 km of crust nearest the trench (Figure 8b). Within layer 2A, this corresponds to an average velocity of 3.6 km/s, 15% porosity, and 5.3 wt.% H_2O.

4.2.2. Upper Crustal Velocity, Porosity, and Water Content Estimates Offshore Sumatra

Sediment velocities offshore Sumatra are very slow in the pelagic section, averaging 1.65 km/s. This is roughly consistent with interval velocities calculated for similar lithologies at DSDP Site 211 to the southwest (von der Borch et al., 1974). These values increase to an average of 1.8 km/s in the turbiditic section and reach more than 2 km/s just above the crust. The 15 km-long streamer provides coverage of the entirety of layers 2A and 2B, as defined by the depth-converted 2A horizon and the ~6.7 km/s contour (e.g., Carlson, 2018). Layer 2A velocities show minor variation across the entire profile, with no systematic decrease toward the trench as observed across AL05, where a far greater number of faults are imaged. Velocity gradients at the top of 2A are very strong, approaching values of 6 s^{-1}, with mean velocities of 3.5 km/s (the same as the average in the bending area along AL05). Velocities average ~5.1 km/s at the 2 A/B transition and approach 6.7–6.8 km/s at the depth limit of resolution (i.e., roughly coinciding with the base of layer 2). This corresponds to average porosities of ~16% (5.4 wt.% H_2O) at the top of the crust, ~5.4% (1.9 wt.% H_2O) at the base of 2A, and values that approach 0 at the base of layer 2 (Figures 8c and 8d). The average velocity within layer 2A is ~4.4 km/s, corresponding to ~9% porosity and ~3.2 wt.% H_2O. Values are ~6.0 km/s, ~2.4% porosity, and ~0.8 wt.% H_2O within layer 2B, and ~5.5 km/s, ~4.4% porosity, and ~1.5 wt.% H_2O for 2.3 km of subducting upper oceanic crust (Table 1).

Velocities are slower in the first 10 km (>55 km from the trench) of the profile, which approaches a large seamount to the southwest, reaching values down to 3 km/s, or up to ~21% porosity and ~7.5 wt.% H_2O at the top of the crust (Figure 6d). Within layer 2B, we observe multiple 5–10 km-wide zones of anomalously low velocities. The largest of these anomalies is observed between 38 and 48 km from the trench, reaching a maximum velocity reduction of ~8% from the model average of 6 km/s to 5.5 km/s (equivalent to an increase from 0.8 to 1.4 wt.% H_2O) around 1.4 km below the basement (Figures 8c and 8d). Similar anomalies are observed in the crust within the first 10 km of the model and between 20–30 km and 5–10 km from the trench. In all cases, these anomalies do not appear to be linked with any obvious fault structures above in the crust and sediments.

5. Discussion

Major differences are seen in the structures and properties of the incoming upper oceanic crust outboard the Alaska and Sumatra trenches despite their similar ages and fast rates at which the crust was accreted. Only a few estimates of upper crustal P-wave velocities in the outer rise exist and are generally of lower resolution than can be achieved using streamer tomography (ref., e.g., Ivandic at al., 2008). Of all the studies that employ the same

methodology of downward continuation and travel-time tomography, the majority focus on young oceanic crust near spreading centers (e.g., Arnulf et al., 2011, 2014a; Henig et al., 2012) or landward of the trench (e.g., Qin & Singh, 2018), with only two recent studies providing estimates for mature oceanic crust (in the Atlantic Ocean: Audhkhasi & Singh, 2019; Kardell et al., 2019). Our study provides some of the first high-resolution estimates of the amount of pore water present in the upper oceanic crust within the outer rise domains of two seismically active subduction zones.

5.1. Hydration State Before Bending

Outside the bending area offshore Alaska, velocities observed at the top of the crust are higher than those found in the bending area (Figure 4b) but are still on the lower end of those observed in situ at DSDP site 1256D for ~16 Myr old oceanic crust (Figure 8a; Carlson, 2014a). This is not surprising, as drilled samples do not encompass large scale porosities (e.g., faults) that are sampled by the seismic waves (e.g., Harding et al., 2016; Jarrard et al., 2003; Wilkens et al., 1991). The average at the top of the crust here (4.1 km/s) is nearly identical to the statistically constant value observed by Audhkhasi and Singh (2019) for mature, slow-spread oceanic crust in the equatorial Atlantic. Conversely, Kardell et al. (2019) report larger values in general for intermediate-to slow-spread crust of similar ages increasing to >4.5 km/s at the top of ~58 Myr old the crust. The discrepancies between both regions could arise from contrasting lithologies of layer 2A (pillows vs. flows; Wilkens et al., 1991) or evolutionary histories between the regions. However, we also cannot rule out differences related to varying regularization parameters used during inversion, such as our use of a larger ratio of horizontal to vertical smoothing weights. On AL05, the smooth basement structure favors the blanketing of sediments that have sealed the top of the crust since at least the lower Oligocene (Creager et al., 1973), and possibly since 3–4 Myr after formation. Given the continuous deposition of pelagic sediments thereafter, we suspect that there could be minimal free water present in the uppermost crust prior to bending on AL05, as these conditions favor the filling of pore spaces through chemical precipitation of mineral phases (e.g., Nedimovic et al., 2008). The bending area offshore Sumatra, which CGGV40 resides entirely within, has less curvature than that offshore Alaska, as well as thinner sediment cover that consists mostly of weakly reflective pelagic sediments (von der Borch et al., 1974) that are eventually overlain by trench fill. This could indicate that the crust was never fully sealed, thus allowing the continued exchange of seawater with time and eventual reopening of cracks due to bending. We also observe a general correlation between basement highs and lows corresponding to locally slower and faster velocities, respectively, along both profiles (Figures 4b and 5b) that could represent the fossilized signature of crustal discharge and recharge (i.e., up-flow and down-flow) (Newman et al., 2011). This implies long wavelength heterogeneities in the amounts of subducting pore and structural water, with basement highs likely containing more pore water prior to bending. This effect is stronger in the upper crust offshore Alaska, where the basement is more undulatory across shorter wavelengths. Thus, layer 2A offshore Sumatra may have held greater amounts of pore water overall prior to bending, though it is difficult to speculate on exact quantities.

5.2. Comparison With Previous Hydration Estimates

While numerous OBS refraction studies performed in the outer rise show similar reductions in upper mantle velocities near the trench (Horning et al., 2016; Ivandic et al., 2008; Shillington et al., 2015; Van Avendonk et al., 2011), they often provide only limited constraints on the velocity structure of the upper to mid oceanic crust. Wide-angle reflection/refraction tomography results obtained perpendicular to the heavily sedimented Cascadia subduction zone show a reduction in upper crustal (0.5–1.5 km below basement) velocities toward the trench that corresponds to as much as ~4 wt.% H_2O; however, layer 2A is not well constrained as ocean-bottom seismometers were spaced at 16 km (Horning et al., 2016). Canales et al. (2017) provide some of the first estimates of both pore and structural water along a trench-parallel profile acquired during the same survey. They report layer 2A (0–370 m below basement) velocities between 4.1 and 4.6 km/s and layer 2B (0.5–1.5 km below basement) velocities between 5.1 and 5.8 km/s, corresponding to ~2.8–3.2 wt.% and 2.3–2.4 wt.% of H_2O, respectively (Table 1). They also calculate the amount of structural water within 2A, which approaches estimates of global averages at ~2 wt.% H_2O that then decreases below expected values within layer 2B down to 0.3 wt.% H_2O (Canales et al., 2017; Carlson, 2003; Peacock, 1990). Ivandic et al. (2008) observe a similar decrease in velocities, most notably in the upper mantle, along an OBS profile near the Middle America Trench offshore Nicaragua, with velocities in the bending area averaging between 4.1 and 4.3 km/s at the top of the basement and

around 6 km/s at the bottom of layer 2 (1.5 km below basement). A recent high-resolution controlled source electromagnetic survey conducted in the same area provides estimates of porosity between ~7.5–12% before bending that increases to ~9–14% on average after bending in 600 m of extrusives. Respectively, these values decrease to 2.7% and 4.8% in the dikes and 0.7% and 1.7% in the gabbros (1.6–5.5 km below basement) (Naif et al., 2015).

Our high-resolution velocity models of the incoming oceanic crust in the outer rise outboard both the Shumagin Gap and Enggano Island suggest the presence of significant amounts of free water trapped in basaltic pores (Table 1). Velocities are slower than those reported in the uppermost crust in most previous studies (e.g., Ivandic et al., 2008; Van Avendonk et al., 2011), and exhibit much higher vertical velocity gradients within layer 2A than are usually captured in OBS models. The estimated porosity values averaged within layer 2A (540 m thick) before (4.7 km/s, 8.0% porosity, or 2.8 wt.% H_2O) and after bending (4.2 km/s, 11% porosity, or 3.9 wt.% H_2O) on AL05 agree well with the lower bounds reported by Naif et al. (2015) offshore Nicaragua. Average layer 2A (640 m thick) values on CGGV40 (4.4 km/s, 9% porosity, or 3.2 wt.% H_2O) are more like estimates made offshore Cascadia (Canales et al., 2017), indicating that the upper crust in the bending area here could be just as saturated as that offshore Alaska. Layer 2B exhibits much greater variability across the profile, with average values again resembling those in the bending area on AL05 down to ~1.3 km below the basement (Figures 8c and 8d). Our estimate of pore water within layer 2B (0.8 wt.% H_2O) appears much lower than is reported offshore Cascadia and Nicaragua, in part because we assume a thicker layer 2B. Taking a similar thickness for layer 2B (~1 km) increases the average to 1.3 wt.% H_2O which increases to ~1.8 wt.% H_2O where the low velocity anomalies are observed. Beneath the largest low-velocity zone within Layer 2B (43–46 km from the trench, Figure 5), values remain well below average down to the depth extent of resolution, suggesting a continuation of this hydration with depth, which may not be the case everywhere. Thus, while layer 2B appears to contain anomalous amounts of free water, the hydration of this layer is more localized and of a slightly lesser degree overall than what has been inferred elsewhere.

5.3. Contrasting Deformation Styles Between Alaska and Sumatra

While the apparent degrees of hydration in the outer rise are similar between both profiles, we observe contrasting structural features that may have contributed to differing styles of deformation affecting the crust. Prior to bending on AL05, the sediment column and upper crust show little to no signs of disruption indicating a fairly straightforward evolution. The main mode of deformation is related to the bending of the plate, which has produced a dense system of normal faults, facilitating the reintroduction of seawater into the crust. Although we do not observe the same focusing of fluids within the crust as is clearly seen in resistivity images (Naif et al., 2015), and which is favored by numerical models (Faccenda, 2014), this could be due to the inherent smoothing effect of travel-time tomography (Van Avendonk et al., 1998). Indeed, checkerboard tests indicate that we are unable to recover well velocity anomalies smaller than 4–5 km wide (Figures S5 and S6 in Supporting Information S1) whereas fault damage zones are expected to be hundreds of meters to a few kilometers wide (Cochran et al., 2009). Additionally, our decision to specify a ratio of horizontal to vertical derivative smoothing weights of 6 during travel-time inversion does not seem to preclude the recovery of obvious structure that may be linked to these faults (Figure S7 in Supporting Information S1). Rather, our preferred models resolve well the vertical velocity gradients required to produce the triplicated arrivals in layer 2 while also capturing the long wavelength velocity structures. Therefore, given the coincident reduction in upper mantle velocities along AL05 reported by Shillington et al. (2015), we believe that bending faults in the outer rise outboard the Shumagin Gap create pathways for fluids to hydrate the crust and penetrate down into the uppermost mantle.

Offshore Enggano Island, the curvature of the down going plate is much less pronounced, and very few bending faults are observed (Figure 2b), meaning hydration of oceanic crust in this area cannot be explained through bending related faulting. We interpret the more localized velocity reductions to be associated with the extensive active deformation currently taking place in the Wharton Basin, east of the Ninetyeast Ridge (Figure 1b). A large diffuse zone of deformation exists within the Indian Ocean (Bull & Scrutton, 1990) that is further complicated by the subduction of the Indo-Australian plate beneath the Sunda plate to the east. In the Wharton Basin, this complex deformation consists of N-S striking fracture zones and a conjugate system of shear zones that are visible in bathymetry data and reflection images (Hananato et al., 2018; Singh et al., 2017). While the reactivation of these fracture zones often produces large basement offsets, there is not always a strong expression at the seafloor,

as may be the case on CGGV40 (Figure 2b; Carton et al., 2014). Therefore, the oceanic crust here could have experienced active deformation that allows water to penetrate deeper (into layer 2B) than is normally the case through hydrothermal circulation alone.

5.4. Downdip Implications of Subducting Hydrated Oceanic Crust

Crustal hydration is believed to influence numerous subduction zone processes, including plate coupling and the generation of large earthquakes (Bilek & Lay, 2018). The state in which water is present (either free or mineral-bound) determines the depth at which it is released, with free water being released at shallower depths along the megathrust, and mineral-bound water being expelled at greater depths beneath the mantle wedge and beyond (e.g., Faccenda, 2014; Hacker et al., 2003). Given the relatively cold thermal structure of both subduction zones, structurally bound water is not likely to be expelled before at least 70 km depth (Abers et al., 2017; van Keken et al., 2011). Therefore, the dewatering of hydrous bound minerals is not likely to influence megathrust properties in the seismogenic zone but could impact arc magmatism and intermediate-depth earthquakes through dehydration embrittlement (e.g., Hacker et al., 2003). Using an altered basalt host lithology (Carlson, 2014b) to calculate porosity allows us to assume all the pores are saturated with seawater, which makes sense given that both areas are actively deforming (Figure 2). However, this assumption means that our estimates likely represent upper bounds on the amount of free water present in the uppermost crust, especially offshore Sumatra where the timing of hydration is less clear. Additionally, if layer 2B is a lithologic layer (i.e., diabase host rock), then our estimates of porosity there could be slightly underestimated (Figure 7).

Analyses of seismicity with depth and isotopic ratios of arc lavas suggest that dehydration downdip of AL05 is confined primarily to the downgoing crust and uppermost mantle, extending down to 150–200 km depth, implying the presence of hydrous bearing minerals (Wei et al., 2021). More intermediate-depth earthquakes appear at depths greater than 120 km in the Shumagin gap compared to neighboring segments, in support of the inferred serpentinization of the upper mantle by Shillington et al. (2015); however, our results only provide an estimate of the amount of free water present in the upper crust. The relatively high amount of free water stored in the uppermost crust, once subducted, might influence the megathrust slip behavior (e.g., Saffer & Tobin, 2011). It has been showed at other subduction zones worldwide that weakly coupled regions appear to correlate with fluid-enriched portions of the megathrust (Saffer, 2017). To date, in the Shumagin segment, weak geodetic coupling has been proposed to arise from the thin and heterogeneous sediment cover and heterogenous plate boundary introduced by bending-related faults (Li et al., 2018; Shillington et al., 2015). However, our study shows that the free water stored in the uppermost crust might also influence megathrust slip behavior there. As the plate boundary subducts to greater depths and temperature increases, it is likely that some of the free fluids react with the host rocks to form hydrous minerals, though quantifying this process would require more data. Hydrous minerals will be carried to greater depths and the releasing of free water through dehydration reactions would occur around 80–100 km depths (Abers et al., 2020). This would be in agreement with higher water content found in the arc lavas of the Shumagin gap volcanoes (Wei et al., 2021). Decaying seafloor spreading magnetic anomalies in this region suggests that bending faults in the Central Aleutians allow for the rejuvenation of hydrothermal circulation near the trench, a process that subsequently alters magnetic minerals in the crust (Choe & Dyment, 2021). Thus, we propose that on AL05, the thinning sediment cover and heterogeneity of the plate boundary near the trench (Figure 2a) facilitates the open exchange of seawater within the uppermost crust. This, along with deformation of the upper plate and heterogeneity of the plate boundary, could contribute to the weak coupling in the region and elevated seismicity at all depths (Li et al., 2018; Shillington et al., 2015)

Conversely, offshore Sumatra, the lack of a dense system of bending related faults coupled with the progressive thickening of the sediment cover (up to 1 km) means there are fewer direct pathways for seawater to come in contact with the crust near the trench axis (Figure 2b). The active circulation of seawater may therefore be confined to the sediments and uppermost crust within 20–30 km from the trench and may persist farther away from the trench in the crust covered by a thin layer of pelagic sediments. A recent GPS study around Enggano Island suggests the presence of an ongoing multiyear slow-slip event (SSE) on the shallow megathrust beneath the island (Mallick et al., 2021). This phenomenon supports the presence of fluids in a subducting sediment channel, the latter of which has been observed to the north near the Mentawai islands (Qin & Singh, 2018). To explain this long-lived SEE, the authors propose a model consisting of increased pore fluid pressure in fault gouge along the shallow portion of the megathrust. Here we propose that the high porosities throughout layer 2A

and 2B could contribute to explaining the presence of this SSE just downdip of CGGV40 like recently proposed for the Hikurangi subduction zone (Chesley et al., 2021). Because deformation in the Wharton basin could have persisted for many millions of years far away from the trench, it is possible that the uppermost crust along CGGV40 contains significant amounts of water as a result. Rather than pervasively hydrating the crust, the hydration within layer 2B appears localized within multiple 5-10 km-wide zones. Localized hydration is suggested to increase the upward flux of water beneath the forearc and arc whereas water stored in a more homogeneous manner is expected to be carried to greater depths (Wada et al., 2012).

6. Conclusion

Recent advances in the processing of multichannel seismic data allow for the recovery of oceanic crustal velocity models at unprecedented resolutions. We apply these techniques to high-quality datasets acquired seaward of segments belonging to the Alaskan and Sumatran subduction zones to provide some of the first high-resolution constraints on the porosity and water content of fast-spread, mature upper oceanic crust in the outer rise. Our model offshore Alaska, AL05, yields good coverage throughout oceanic layer 2A both before and after bending, while our model offshore Sumatra, CGGV40, provides information on the entirety of layer 2 within the bending area. We observe anomalously low velocities within layer 2A in the bending area along both profiles which implies elevated quantities of free water; however, the dominant mode of deformation through which the crust is rehydrated is likely not the same in both regions. Outboard the Shumagin Gap, the curvature of the downgoing plate and favorably oriented pre-existing fabric produce a dense system of bending related faults that extend down into the uppermost mantle and is coupled with a thinning sediment cover toward the trench. This leads to the rejuvenation of open hydrothermal circulation in the crust, and as the crust subducts and temperature increases, some of the free water can be expelled or react with the host rocks to form hydrous minerals that are carried down to sub-arc depths and beyond, impacting both arc magmatism and intermediate-depth seismicity. Offshore Enggano Island, the crust appears equally as hydrated despite the lack of abundant bending faults. We suggest that this is linked to the ongoing complex deformation of the Indo-Australian plate, more subtle plate bending than in Alaska and lack of thick sedimentary cover away from the trench that never fully seals the basement. These results are consistent with the observation of a slow slip beneath Enggano Island that requires dewatering along the shallow megathrust as well as the imaging of a large, intact subducted seamount that favors a weak coupling of the plate interface.

Data Availability Statement

Raw Seismic reflection data from this study are available through the Marine Geoscience Data System (http://www.marine-geo.org/tools/entry/MGL1110).

Acknowledgments

We gratefully acknowledge the captain and crew of the R/V Marcus G. Langseth for their efforts during the ALEUT experiment offshore Alaska. The CGG40 profile data were acquired on board the CGG vessel Geowave Champion and was fully funded by CGG. We are grateful to Suzanne Carbotte, Brandon Shuck and Rick Carlson for helpful feedback discussions. We would also like to thank the Associate Editor, Dominik Kardell and one anonymous reviewer who provided excellent feedback that greatly improved this Manuscript. We also thank Shearwater Geoservices for providing an academic license to use the Reveal seismic processing software. This research was supported by the National Science Foundation through NSF award OCE-1634625 at LDEO-Columbia University.

References

Abercrombie, R. E., Antolik, M., & Ekström, G. (2003). The June 2000 Mw 7.9 earthquakes south of sumatra: Deformation in the India–Australia plate. *Journal of Geophysical Research*, *108*(B1), ESE6-1–ESE6-16. https://doi.org/10.1029/2001JB000674

Abers, G. A., Van Keken, P. E., & Hacker, B. R. (2017). The cold and relatively dry nature of mantle forearcs in subduction zones. *Nature Geoscience*, *10*(5), 333–337. https://doi.org/10.1038/ngeo2922

Abers, G. A., Van Keken, P. E., & Wilson, C. R. (2020). Deep decoupling in subduction zones: Observations and temperature limits. *Geosphere*, *16*(6), 1408–1424. https://doi.org/10.1130/GES02278.1

Alt, J. C. (1995). Subseafloor processes in mid-ocean ridge hydrothennal systems. In *Seafloor hydrothermal systems: Physical, chemical, biological, and geological interactions* (pp. 85–114). American Geophysical Union (AGU). https://doi.org/10.1029/GM091p0085

Arnulf, A. F., Harding, A., Singh, S., Kent, G., & Crawford, W. (2014). Nature of upper crust beneath the lucky strike volcano using elastic full waveform inversion of streamer data. *Geophysical Journal International*, *196*(3), 1471–1491. https://doi.org/10.1093/gji/ggt461

Arnulf, A. F., Harding, A. J., Kent, G. M., Singh, S. C., & Crawford, W. C. (2014b). Constraints on the shallow velocity structure of the lucky strike volcano, mid-atlantic ridge, from downward continued multichannel streamer data. *Journal of Geophysical Research: Solid Earth*, *119*(2), 1119–1144. https://doi.org/10.1002/2013jb010500

Arnulf, A. F., Singh, S. C., Harding, A. J., Kent, G. M., & Crawford, W. (2011). Strong seismic heterogeneity in layer 2a near hydrothermal vents at the mid-Atlantic ridge. *Geophysical Research Letters*, *38*(13). https://doi.org/10.1029/2011gl047753

Audhkhasi, P., & Singh, S. C. (2019). Seismic structure of the upper crust from 0–75 ma in the equatorial atlantic ocean on the african plate using ultralong offset seismic data. *Geochemistry, Geophysics, Geosystems*, *20*(12), 6140–6162. https://doi.org/10.1029/2019GC008577

Bécel, A., Shillington, D. J., Delescluse, M., Nedimović, M. R., Abers, G., Saffer, D. M., et al. (2017). Tsunamigenic structures in a creeping section of the Alaska subduction zone. *Nature Geoscience*, *10*, 609. https://doi.org/10.1038/ngeo2990

Bécel, A., Shillington, D. J., Nedimović, M. R., Webb, S. C., & Kuehn, H. (2015). Origin of dipping structures in fast-spreading oceanic lower crust offshore Alaska imaged by multichannel seismic data. *Earth and Planetary Science Letters*, *424*, 26–37. https://doi.org/10.1016/j.epsl.2015.05.016

Berryhill, J. R. (1979). Wave-equation datuming. *Geophysics*, *44*(8), 1329–1344. https://doi.org/10.1190/1.1441010

Berryhill, J. R. (1984). Wave-equation datuming before stack. *Geophysics*, *49*(11), 2064–2066. https://doi.org/10.1190/1.1441620

Bilek, S. L., & Lay, T. (2018). Subduction zone megathrust earthquakes. *Geosphere*, *14*(4), 1468–1500. https://doi.org/10.1130/GES01608.1

Bock, Y., Prawirodirdjo, L., Genrich, J. F., Stevens, C. W., McCaffrey, R., Subarya, C., et al. (2003). Crustal motion in Indonesia from global positioning system measurements. *Journal of Geophysical Research*, *108*(B8). https://doi.org/10.1029/2001JB000324

Bull, J. M., & Scrutton, R. A. (1990). Fault reactivation in the central Indian Ocean and the rheology of oceanic lithosphere. *Nature*, *344*(6269), 855–858. https://doi.org/10.1038/344855a0

Cai, C., Wiens, D. A., Shen, W., & Eimer, M. (2018). Water input into the mariana subduction zone estimated from ocean-bottom seismic data. *Nature*, *563*(7731), 389–392. https://doi.org/10.1038/s41586-018-0655-4

Canales, J. P., Carbotte, S. M., Nedimović, M. R., & Carton, H. (2017). Dry juan de fuca slab revealed by quantification of water entering cascadia subduction zone. *Nature Geoscience*, *10*(11), 864–870. https://doi.org/10.1038/ngeo3050

Carlson, R. L. (2003). Bound water content of the lower oceanic crust estimated from modal analyses and seismic velocities of oceanic diabase and gabbro. *Geophysical Research Letters*, *30*(22). https://doi.org/10.1029/2003GL018213

Carlson, R. L. (2010). How crack porosity and shape control seismic velocities in the upper oceanic crust: Modeling downhole logs from holes 504b and 1256d. *Geochemistry, Geophysics, Geosystems*, *11*(4). https://doi.org/10.1029/2009GC002955

Carlson, R. L. (2014a). The effects of alteration and porosity on seismic velocities in oceanic basalts and diabases. *Geochemistry, Geophysics, Geosystems*, *15*(12), 4589–4598. https://doi.org/10.1002/2014GC005537

Carlson, R. L. (2014b). The influence of porosity and crack morphology on seismic velocity and permeability in the upper oceanic crust. *Geochemistry, Geophysics, Geosystems*, *15*(1), 10–27. https://doi.org/10.1002/2013GC004965

Carlson, R. L. (2018). Ocean crustal seismic layer 2c. *Geochemistry, Geophysics, Geosystems*, *19*(9), 3084–3096. https://doi.org/10.1029/2018GC007614

Carton, H., Singh, S. C., Hananto, N. D., Martin, J., Djajadihardja, Y. S., Udrekh, et al. (2014). Deep seismic reflection images of the wharton basin oceanic crust and uppermost mantle offshore northern sumatra: Relation with active and past deformation. *Journal of Geophysical Research: Solid Earth*, *119*(1), 32–51. https://doi.org/10.1002/2013JB010291

Chesley, C., Naif, S., Key, K., & Bassett, D. (2021). Fluid-rich subducting topography generates anomalous forearc porosity. *Nature*, *595*(7866), 255–260. https://doi.org/10.1038/s41586-021-03619-8

Chlieh, M., Avouac, J. P., Sieh, K., Natawidjaja, D. H., & Galetzka, J. (2008). Heterogeneous coupling of the sumatran megathrust constrained by geodetic and paleogeodetic measurements. *Journal of Geophysical Research*, *113*(B5). https://doi.org/10.1029/2007JB004981

Choe, H., & Dyment, J. (2021). The fate of marine magnetic anomaly in subduction zones: A global appraisal. *Earth and Planetary Science Letters*, *561*, 116787. https://doi.org/10.1016/j.epsl.2021.116787

Christeson, G. L., Goff, J. A., & Reece, R. S. (2019). Synthesis of oceanic crustal structure from two dimensional seismic profiles. *Reviews of Geophysics*, *57*(2), 504–529. https://doi.org/10.1029/2019RG000641

Cochran, E. S., Li, Y.-G., Shearer, P. M., Barbot, S., Fialko, Y., & Vidale, J. E. (2009). Seismic and geodetic evidence for extensive, long-lived fault damage zones. *Geology*, *37*(4), 315–318. https://doi.org/10.1130/G25306A.1

Collier, J. S., & Singh, S. C. (1997). Detailed structure of the top of the melt body beneath the east Pacific rise at 9°40'n from waveform inversion of seismic reflection data. *Journal of Geophysical Research*, *102*(B9), 20287–20304. https://doi.org/10.1029/97JB01514

Collier, J. S., & Singh, S. C. (1998). Poisson's ratio structure of young oceanic crust. *Journal of Geophysical Research*, *103*(B9), 20981–20996. https://doi.org/10.1029/98jb01980

Creager, J. S., Scholl, D. W., & Supko, P. R. (1973). In *Deep sea drilling project initial report, Leg 19: Initial reports of the deep sea drilling project* (Vol. 19). U.S Government Printing Office.

Crowell, B. W., & Melgar, D. (2020). Slipping the shumagin gap: A kinematic coseismic and early afterslip model of the mw 7.8 Simeonof island, Alaska, earthquake. *Geophysical Research Letters*, *47*(19), e2020GL090308. https://doi.org/10.1029/2020GL090308

Davies, J., Sykes, L., House, L., & Jacob, K. (1981). Shumagin seismic gap, Alaska peninsula: History of great earthquakes, tectonic setting, and evidence for high seismic potential. *Journal of Geophysical Research*, *86*(B5), 38213855. https://doi.org/10.1029/JB086iB05p03821

Engebretson, D. C., Cox, A., & Gordon, R. G. (1984). Relative motions between oceanic plates of the Pacific basin. *Journal of Geophysical Research*, *89*(B12), 10291–10310. https://doi.org/10.1029/JB089iB12p10291

Estep, J., Reece, R., Kardell, D. A., Perez, N. D., Christeson, G. L., & Carlson, R. L. (2020). Intraplate deformation of oceanic crust near the rio grande rise in the south atlantic. *Tectonophysics*, *790*, 228543. https://doi.org/10.1016/j.tecto.2020.228543

Faccenda, M. (2014). Water in the slab: A trilogy. *Tectonophysics*, *614*, 1–30. https://doi.org/10.1016/j.tecto.2013.12.020

Fitch, T. J. (1972). Plate convergence, transcurrent faults, and internal deformation adjacent to southeast Asia and the Western Pacific. *Journal of Geophysical Research*, *77*(23), 4432–4460. https://doi.org/10.1029/JB077i023p04432

Fournier, T. J., & Freymueller, J. T. (2007). Transition from locked to creeping subduction in the shumagin region, Alaska. *Geophysical Research Letters*, *34*(6). https://doi.org/10.1029/2006GL029073

Fujie, G., Miura, S., Kodaira, S., Kaneda, Y., Shinohara, M., Mochizuki, K., et al. (2013). Along trench structural variation and seismic coupling in the northern Japan subduction zone. *Earth Planets and Space*, *65*(2), 75–83. https://doi.org/10.5047/eps.2012.06.003

Grevemeyer, I., Ranero, C. R., Flueh, E. R., Kläschen, D., & Bialas, J. (2007). Passive and active seismological study of bending-related faulting and mantle serpentinization at the middle America trench. *Earth and Planetary Science Letters*, *258*(3), 528–542. https://doi.org/10.1016/j.epsl.2007.04.013

Hacker, B. R., Peacock, S. M., Abers, G. A., & Holloway, S. D. (2003). Subduction factory 2. Are intermediate-depth earthquakes in subducting slabs linked to metamorphic dehydration reactions? *Journal of Geophysical Research*, *108*(B1). https://doi.org/10.1029/2001JB001129

Hananto, N., Boudarine, A., Carton, H., Singh, S. C., Avianto, P., Dyment, J., et al. (2018). Evidence of pervasive trans-tensional deformation in the northwestern wharton basin in the 2012 earthquakes rupture area. *Earth and Planetary Science Letters*, *502*, 174–186. https://doi.org/10.1016/j.epsl.2018.09.007

Harding, A. J., Arnulf, A. F., & Blackman, D. K. (2016). Velocity structure near iodp hole u1309d, atlantis massif, from waveform inversion of streamer data and borehole measurements. *Geochemistry, Geophysics, Geosystems*, *17*(6), 1990–2014. https://doi.org/10.1002/2016GC006312

Harding, A. J., Kent, G. M., & Orcutt, J. A. (1993). A multichannel seismic investigation of upper crustal structure at 9°n on the east Pacific rise: Implications for crustal accretion. *Journal of Geophysical Research*, *98*(B8), 13925–13944. https://doi.org/10.1029/93JB00886

Henig, A. S., Blackman, D. K., Harding, A. J., Canales, J.-P., & Kent, G. M. (2012). Downward continued multichannel seismic refraction analysis of Atlantis massif oceanic core complex, 30°n, mid-Atlantic ridge. *Geochemistry, Geophysics, Geosystems*, *13*(5). https://doi.org/10.1029/2012GC004059

Herman, M., & Furlong, K. (2021). Triggering an unexpected earthquake in an uncoupled subduction zone. *Science Advances*, *7*, eabf7590. https://doi.org/10.1126/sciadv.abf7590

Horning, G., Canales, J. P., Carbotte, S. M., Han, S., Carton, H., Nedimović, M. R., & Van Keken, P. E. (2016). A 2-d tomographic model of the juan de fuca plate from accretion at axial seamount to subduction at the cascadia margin from an active source ocean bottom seismometer survey. *Journal of Geophysical Research: Solid Earth*, *121*(8), 5859–5879. https://doi.org/10.1002/2016JB013228

Ivandic, M., Grevemeyer, I., Berhorst, A., Flueh, E. R., & McIntosh, K. (2008). Impact of bending related faulting on the seismic properties of the incoming oceanic plate offshore of Nicaragua. *Journal of Geophysical Research*, *113*(B5). https://doi.org/10.1029/2007JB005291

Jacob, J., Dyment, J., & Yatheesh, V. (2014). Revisiting the structure, age, and evolution of the wharton basin to better understand subduction under Indonesia. *Journal of Geophysical Research: Solid Earth*, *119*(1), 169–190. https://doi.org/10.1002/2013JB010285

Jarrard, R. D., Abrams, L. J., Pockalny, R., Larson, R. L., & Hirono, T. (2003). Physical properties of upper oceanic crust: Ocean drilling program hole 801c and the waning of hydrothermal circulation. *Journal of Geophysical Research*, *108*(B4). https://doi.org/10.1029/2001jb001727

Jimenez-Tejero, C. E., Ranero, C. R., Sallares, V., & Gras, C. (2022). Downward continuation of marine seismic reflection data: An undervalued tool to improve velocity models. *Geophysical Journal International*, *230*(2), 831–848. https://doi.org/10.1093/gji/ggac087

Johnson, J. M., & Satake, K. (1994). Rupture extent of the 1938 Alaskan earthquake as inferred from tsunami waveforms. *Geophysical Research Letters*, *21*(8), 733–736. https://doi.org/10.1029/94GL00333

Kardell, D. A., Christeson, G. L., Estep, J. D., Reece, R. S., & Carlson, R. L. (2019). Long-lasting evolution of layer 2a in the Western south Atlantic: Evidence for low-temperature hydrothermal circulation in old oceanic crust. *Journal of Geophysical Research: Solid Earth*, *124*(3), 2252–2273. https://doi.org/10.1029/2018jb016925

Kardell, D. A., Zhao, Z., Ramos, E. J., Estep, J., Christeson, G. L., Reece, R. S., & Hesse, M. A. (2021). Hydrothermal models constrained by fine-scale seismic velocities confirm hydrothermal cooling of 7–63 ma south Atlantic crust. *Journal of Geophysical Research: Solid Earth*, *126*(6), e2020JB021612. https://doi.org/10.1029/2020JB021612

Konca, A. O., Avouac, J.-P., Sladen, A., Meltzner, A. J., Sieh, K., Fang, P., et al. (2008). Partial rupture of a locked patch of the sumatra megathrust during the 2007 earthquake sequence. *Nature*, *456*(7222), 631–635. https://doi.org/10.1038/nature07572

Li, J., Shillington, D. J., Saffer, D. M., Becel, A., Nedimović, M. R., Kuehn, H., et al. (2018). Connections between subducted sediment, pore-fluid pressure, and earthquake behavior along the Alaska megathrust. *Geology*, *46*, 299–302. https://doi.org/10.1130/G39557.1

Li, S., & Freymueller, J. T. (2018). Spatial variation of slip behavior beneath the Alaska peninsula along Alaska-aleutian subduction zone. *Geophysical Research Letters*, *45*(8), 3453–3460. https://doi.org/10.1002/2017GL076761

López, A. M., & Okal, E. A. (2006). A seismological reassessment of the source of the 1946 Aleutian 'tsunami' earthquake. *Geophysical Journal International*, *165*(3), 835–849. https://doi.org/10.1111/j.1365-246X.2006.02899.x

Mallick, R., Meltzner, A. J., Tsang, L. L. H., Lindsey, E. O., Feng, L., & Hill, E. M. (2021). Long-lived shallow slow-slip events on the sunda megathrust. *Nature Geoscience*, *14*(5), 327–333. https://doi.org/10.1038/s41561-021-00727-y

Masson, D. (1991). Fault patterns at outer trench walls. *Marine Geophysical Researches*, *14*, 209–225. https://doi.org/10.1007/BF00369150

Miller, N. C., & Lizarralde, D. (2016). Finite-frequency wave propagation through outer rise fault zones and seismic measurements of upper mantle hydration. *Geophysical Research Letters*, *43*(15), 7982–7990. https://doi.org/10.1002/2016GL070083

Moser, T. J. (1991). Shortest path calculation of seismic rays. *Geophysics*, *56*(1), 59–67. https://doi.org/10.1190/1.1442958

Naif, S., Key, K., Constable, S., & Evans, R. L. (2015). Water-rich bending faults at the middle America trench. *Geochemistry, Geophysics, Geosystems*, *16*(8), 2582–2597. https://doi.org/10.1002/2015GC005927

Natawidjaja, D. H., Sieh, K., Chlieh, M., Galetzka, J., Suwargadi, B. W., Cheng, H., et al. (2006). Source parameters of the great sumatran megathrust earthquakes of 1797 and 1833 inferred from coral microatolls. *Journal of Geophysical Research*, *111*(B6), a–n. https://doi.org/10.1029/2005JB004025

Nedimović, M. R., Carbotte, S. M., Diebold, J. B., Harding, A. J., Canales, J. P., & Kent, G. M. (2008). Upper crustal evolution across the juan de fuca ridge flanks. *Geochemistry, Geophysics, Geosystems*, *9*(9). https://doi.org/10.1029/2008GC002085

Newman, K. R., Nedimović, M. R., Canales, J. P., & Carbotte, S. M. (2011). Evolution of seismic layer 2b across the juan de fuca ridge from hydrophone streamer 2-d traveltime tomography. *Geochemistry, Geophysics, Geosystems*, *12*(5), a–n. https://doi.org/10.1029/2010GC003462

Peacock, S. A. (1990). Fluid processes in subduction zones. *Science*, *248*(4953), 329–337. https://doi.org/10.1126/science.248.4953.329

Prawirodirdjo, L., McCaffrey, R., Chadwell, C. D., Bock, Y., & Subarya, C. (2010). Geodetic observations of an earthquake cycle at the sumatra subduction zone: Role of interseismic strain segmentation. *Journal of Geophysical Research*, *115*(B3). https://doi.org/10.1029/2008JB006139

Qin, Y., & Singh, S. C. (2018). Insight into frontal seismogenic zone in the mentawai locked region from seismic full waveform inversion of ultralong offset streamer data. *Geochemistry, Geophysics, Geosystems*, *19*(11), 4342–4365. https://doi.org/10.1029/2018gc007787

Ranero, C. R., Phipps Morgan, J., McIntosh, K., & Reichert, C. (2003). Bending-related faulting and mantle serpentinization at the middle America trench. *Nature*, *425*(6956), 367–373. https://doi.org/10.1038/nature01961

Rüpke, L. H., Morgan, J. P., Hort, M., & Connolly, J. A. (2004). Serpentine and the subduction zone water cycle. *Earth and Planetary Science Letters*, *223*(1), 17–34. https://doi.org/10.1016/j.epsl.2004.04.018

Ryan, W. B. F., Carbotte, S. M., Coplan, J. O., O'Hara, S., Melkonian, A., Arko, R., et al. (2009). Global multi-resolution topography synthesis. *Geochemistry, Geophysics, Geosystems*, *10*(3), a–n. https://doi.org/10.1029/2008GC002332

Saffer, D. M. (2017). Mapping fluids to subduction megathrust locking and slip behavior. *Geophysical Research Letters*, *44*(18), 9337–9340. https://doi.org/10.1002/2017GL075381

Saffer, D. M., & Tobin, H. J. (2011). Hydrogeology and mechanics of subduction zone forearcs: Fluid flow and pore pressure. *Annual Review of Earth and Planetary Sciences*, *39*(1), 157–186. https://doi.org/10.1146/annurev-earth-040610-133408

Sella, G. F., Dixon, T. H., & Mao, A. (2002). Revel: A model for recent plate velocities from space geodesy. *Journal of Geophysical Research*, *107*(B4), 11–1. ETG 11-1-ETG 11. https://doi.org/10.1029/2000JB000033

Shillington, D. J., Bécel, A., Nedimović, M. R., Kuehn, H., Webb, S. C., Abers, G. A., et al. (2015). Link between plate fabric, hydration and subduction zone seismicity in Alaska. *Nature Geoscience*, *8*(12), 961–964. https://doi.org/10.1038/ngeo2586

Sieh, K., & Natawidjaja, D. (2000). Neotectonics of the sumatran fault, Indonesia. *Journal of Geophysical Research*, *105*(B12), 28295–28326. https://doi.org/10.1029/2000JB900120

Singh, S. C., Hananto, N., Mukti, M., Permana, H., Djajadihardja, Y., & Harjono, H. (2011). Seismic images of the megathrust rupture during the 25th october 2010 pagai earthquake, sw sumatra: Frontal rupture and large tsunami. *Geophysical Research Letters*, *38*(16), a–n. https://doi.org/10.1029/2011GL048935

Singh, S. C., Hananto, N., Mukti, M., Robinson, D. P., Das, S., Chauhan, A., et al. (2011). Aseismic zone and earthquake segmentation associated with a deep subducted seamount in sumatra. *Nature Geoscience*, *4*(5), 308311. https://doi.org/10.1038/ngeo1119

Singh, S. C., Hananto, N., Qin, Y., Leclerc, F., Avianto, P., Tapponnier, P., et al. (2017). The discovery of a conjugate system of faults in the wharton basin intraplate deformation zone. *Science Advances*, *3*, 8. https://doi.org/10.1126/sciadv.1601689

Singh, S. C., Hobbs, R. W., & Snyder, D. B. (1996). Broadband receiver response from dual-streamer data and applications in deep reflection seismology. *Geophysics*, *61*(1), 232–243. https://doi.org/10.1190/1.1443944

Stevenson, A. J., Scholl, D. W., & Vallier, T. L. (1983). Tectonic and geologic implications of the Zodiac fan, aleutian abyssal plain, northeast Pacific. *GSA Bulletin*, *94*(2), 259–273. https://doi.org/10.1130/0016-7606(1983)94<259:tagiot>2.0.co;2

Taylor, M. A. J., & Singh, S. C. (2002). Composition and microstructure of magma bodies from effective medium theory. *Geophysical Journal International*, *149*(1), 15–21. https://doi.org/10.1046/j.1365-246X.2002.01577.x

Van Avendonk, H. J. A., Harding, A., Orcutt, J., & Mcclain, J. (1998). A two dimensional tomographic study of the clipperton transform fault. *Journal of Geophysical Research*, *103*, 17885–17899. https://doi.org/10.1029/98JB00904

Van Avendonk, H. J. A., Holbrook, W. S., Lizarralde, D., & Denyer, P. (2011). Structure and serpentinization of the subducting cocos plate offshore Nicaragua and Costa Rica. *Geochemistry, Geophysics, Geosystems*, *12*(6), a–n. https://doi.org/10.1029/2011GC003592

Van Avendonk, H. J. A., Shillington, D. J., Holbrook, W. S., & Hornbach, M. J. (2004). Inferring crustal structure in the aleutian island arc from a sparse wide-angle seismic data set. *Geochemistry, Geophysics, Geosystems*, *5*(8). https://doi.org/10.1029/2003GC000664

Van Keken, P. E., Hacker, B. R., Syracuse, E. M., & Abers, G. A. (2011). Subduction factory: 4. Depth dependent flux of H_2O from subducting slabs worldwide. *Journal of Geophysical Research*, *116*(B1). https://doi.org/10.1029/2010jb007922

Von der Borch, C. C., Sclater, J. G., Gartner, S., Jr., Hekinian, R., Johnson, D. A., McGowran, B., et al. (1974). Site 211. *Initial Reports of the Deep Sea Drilling Project*, *22*, 13. https://doi.org/10.2973/dsdp.proc.22.102.1974

Von Huene, R., & Scholl, D. W. (1991). Observations at convergent margins concerning sediment subduction, subduction erosion, and the growth of continental crust. *Reviews of Geophysics*, *29*(3), 279–316. https://doi.org/10.1029/91RG00969

Wada, I., Behn, M. D., & Shaw, A. M. (2012). Effects of heterogeneous hydration in the incoming. plate, slab rehydration, and mantle wedge hydration on slab derived H_2O flux in subduction zones. *Earth and Planetary Science Letters*, *353–354*, 60–71. https://doi.org/10.1016/j.epsl.2012.07.025

Wei, S. S., Ruprecht, P., Gable, S. L., Huggins, E. G., Ruppert, N., Gao, L., & Zhang, H. (2021). Along strike variations in intermediate-depth seismicity and arc magmatism along the Alaska peninsula. *Earth and Planetary Science Letters*, *563*, 116878. https://doi.org/10.1016/j.epsl.2021.116878

Wilkens, R. H., Fryer, G. J., & Karsten, J. (1991). Evolution of porosity and seismic structure of upper oceanic crust: Importance of aspect ratios. *Journal of Geophysical Research*, *96*(B11), 17981–17995. https://doi.org/10.1029/91jb01454

Ye, L., Bai, Y., Si, D., Lay, T., Cheung, K. F., & Kanamori, H. (2022). Rupture model for the 29 july 2021 mw 8.2 Chignik, Alaska earthquake constrained by seismic, geodetic, and tsunami observations. *Journal of Geophysical Research: Solid Earth*, *127*(7), e2021JB023676. https://doi.org/10.1029/2021JB023676

Ye, L., Lay, T., Kanamori, H., Yamazaki, Y., & Cheung, K. F. (2021). The 22 july 2020 mw 7.8 Shumagin seismic gap earthquake: Partial rupture of a weakly coupled megathrust. *Earth and Planetary Science Letters*, *562*, 116879. https://doi.org/10.1016/j.epsl.2021.116879

Zhang, H., & Thurber, C. H. (2007). Estimating the model resolution matrix for large seismic tomography problems based on Lanczos bidiagonalization with partial reorthogonalization. *Geophysical Journal International*, *170*(1), 337–345. https://doi.org/10.1111/j.1365-246X.2007.03418.x

Zhou, Z., & Lin, J. (2018). Elasto-plastic deformation and plate weakening due to normal faulting in the subducting plate along the mariana trench. *Tectonophysics*, *734–735*, 59–68. https://doi.org/10.1016/j.tecto.2018.04.008

Erratum

In the originally published version of this article, Figure 4 included typographical errors involving faint lines. The errors were purely typographical and the implementation of Figure 4 was unaffected. New Figure 4 was updated. In addition, the Author Contributions list contained typographical errors involving contributions directed to only few authors. The errors have been corrected, and this may be considered the authoritative version of record.